GEORG-AUGUST-UNIVERSITÄT
GÖTTINGEN

Quantifying the evolution of a hydrothermal system using high-resolution low-temperature thermochronology and a numerical model

Master-Thesis

by
Sarah Louis
from Minden, Germany

28.04.2017

Supervisor: Dr. Elco Luijendijk, Dept. of Structural Geology and Geodynamics, Georg-August-Universität Göttingen, Göttingen, Germany

Co-supervisor: Prof. Dr. Mark Person, Dept. of Earth and Environmental Science, New Mexico Tech, Socorro, NM, USA.

Department of Hydrogeology and Environmental Geosciences

Table of contents

TABLE OF FIGURES

ACKNOWLEDGEMENTS

First of all, I'm gratefully thanking my supervisors Dr. Elco Luijendijk and Prof. Mark Person for giving me the opportunity to study this super interesting hydrothermal system and introducing me to the new world of deep hydrothermal systems, thermochronology and computer modeling. Lieve Elco, mijn dank aan jou is bijzonder groot. Je bent de beste begeleider die een student zich wensen kan. Ik heb respekt voor jou onophoudelijke wetenschappelijke niewsgierigheid en jou aanstekelijk enthousiasme voor het werk en jou veelzijdige ideen. Je hebt me niet alleen zonder enige verplichting onderstuund maar ook constant geinspireerd en gemotiveerd. Ik dank je van ganser harte voor je bemoeienis en de vele tijd die jij in het projekt en in mij als studente hebt gestoken. Ook dank ik jou voor het feit dat je mij hebt geholpen met het wetenschappelijke schrijven in een mate die hoger ligt als voor een masterscriptie verlangt word, en voor jou financiele ondersteuning waardoor jij mij het mogelijk gemaakt hebt mijn masterscriptie bij de EGU voor te stellen. Ik blijf je enige IPAs schuldig.

Special thanks are going to Dr. István and Judit Dunkl for their continuous help in the geochronology lab and also for their warm and friendly interactions with their students and colleagues. Kedves István! Ezúton szeretném megköszönni, hogy bevezettél engem a kishőmérsékletű termokronológia rejtelmeibe. Hálás vagyok mindazért a sokért, amit ehhez a projekthez hozzátettél, türelmedet és egyébként szűkös idődet sem sajnálva. Köszönet mindazért a tudásért és tapasztalatért, amit megosztottál velem. Judit, neked pedig különösen hálás vagyok azért, hogy rendíthetetlenül segítettél nekem a sok-sok cirkon és apatit kiválogatásában.

Many thanks to Dr. Volker Karius for guiding me through XRD measurements and for sharing your expertise in data evaluation. Vielen lieben Dank, Volker, für die viele Zeit, die du dir genommen hast um mir die XRD Messung zu zeigen und vor allem für den Aufwand, den du dir mit der Rietveld-Analyse gemacht hast.

Furthermore I am thanking Mathias Hueck for introducing me to the heavy liquid mineral separation and Gwynlyn Buchanan for proof reading my thesis. Thanks to my fellow HEG students for making the past 2 ½ years such a great time and for sticking together during the hurly-burly master courses.

Last but not least, I am so grateful for the support of my friends and family. Beste Oma der Welt: vielen Dank für deine andauernde seelische und körperliche Unterstützung. Ohne dich würde ich heute keine Masterarbeit abgeben können. Ohne dich hätte ich in Göttingen keine zweite Heimat finden dürfen. Und ohne dich wäre der Phin nicht so ein glückseliges Kind geworden. Dafür werde ich dir ein Leben lang verbunden sein. Liebste Mama der Welt: ich danke dir nicht nur für deine Unterstützung bei meiner Arbeit von ganzem Herzen, sondern auch dafür, dass du mir immer wieder die bedingungslose Mamaliebe entgegen bringst, die mein Leben immer wieder lebenswert macht. Papi, ich bin in Gedanken bei dir. Mein allerliebster Phin, du bist mein persönlicher Held. Ich danke dir so sehr für deine Geduld und dein Verständnis; dass du mir nie böse warst, wenn ich so wenig Zeit für dich und so viel Zeit für die Arbeit und das Studium aufgebracht habe. Lieber Marcel, dir möchte ich für deine Geduld und deine aufbauenden Worte und Taten in ruhigen und stressigen Zeiten danken. Und auch für dein Interesse und den wissenschaftlichen Austausch den wir glücklicherweise immer mal wieder haben durften. Bleib so wie du bist. Liebste Laura, nichts geht über die beste Luppifreundschaft. Es ist so schön, die feste Gewissheit zu haben, dass es immer einen Menschen gibt, der mich auffängt. Und dieser besondere Mensch in meinem Leben bist seit nun mehr als 27 Jahren du. Schön, dass wir in den letzten zwei Jahren einen kleinen Lebensabschnitt Seite an Seite in Göttingen verbringen durften.

ZUSAMMENFASSUNG

Es ist eine Herausforderung, die Entstehungsgeschichte von hydrothermalen Systemen und heißen Quellen zu quantifizieren, da es oft schwierig ist, hydrothermale Ablagerungen in ausreichender Auflösung zu datieren. Um Aufschluss darüber zu erlangen, wie geologische Prozesse wie z.B. Erdbeben und Verwerfungen mit Fluidströmungen interagieren, ist es jedoch wichtig, hydrothermale Aktivität quantifizieren zu können. In dieser Arbeit werden (U-Th)/He Datensätze mit einem numerischen Wärmeflussmodell kombiniert, um die Entstehungsgeschichte eines aktiven hydrothermalen Systems zu bestimmen. Dazu wurden Oberflächengesteinsproben um eine hydrothermal aktive Abschiebung in Beowawe (Nevada, USA) gesammelt und deren Apatit-Helium-Alter (AHe) bestimmt. Das Apatit-Helium-Alter der Proben aus der unmittelbaren Umgebung der heißen Quellen und Geysiere weisten eine signifikante thermale Überprägung auf. Gesteinsproben welche in einem größeren Abstand von ca. 50m entnommen wurden, sind von der hydrothermalen Aktivität unbeeinflusst. Deren AHe-Alter gleichen dem U-Pb-Alter des vulkanischen Muttergesteins von 15.6 Ma. Die beobachtete hydrothermale Überprägung entstand durch die ins Gestein geleiteten hohen Temperaturen (~95°C) der hydrothermalen Fluide, welche über lange Zeiträume entlang der Malpais-Abschiebung abflossen. Die Größe der thermisch beeinflussten Fläche hängt von der Dauer der hydrothermalen Aktivität ab; je länger das System aktiv war, desto größer ist die thermische Aureole um die Abschiebung herum. Um die Dauer der hydrothermalen Aktivität mittels AHe-Daten zu bestimmen, wurde ein numerisches Modell, welches auf advektivem und leitendem Wärmefluss basiert, benutzt. Die Kombinierung von Niedrigtemperatur-Thermochronometern mit einem thermischen Modell kann daher zur Quantifizierung von hydrothermaler Aktivität über geologische Zeiträume hinweg dienen.

ABSTRACT

Quantifying the history of hydrothermal systems and hot springs is challenging because hydrothermal deposits are often difficult to date at sufficient resolution. However, the quantification of hydrothermal activity is important for gaining insights on how geological processes, such as earthquakes and faulting, interact with fluid flow. Here we combine high-density apatite (U-Th)/He data with a numerical model of heat flow to determine the history of an active hydrothermal system. We measured apatite-helium (AHe) ages of surface rock samples collected around a hydrothermally active normal fault in Beowawe (Nevada,USA). AHe ages in the vicinity of the hot springs along the fault showed significant thermal overprint. Samples located at a distance of ~50m were unaffected by hydrothermal activity and showed AHe ages that were equal to the U-Pb age of the volcanic host rock of 15.6 Ma. The observed thermal overprint is caused by high temperatures (~95°C) of the hydrothermal fluids along the Malpais fault that have heated the adjacent rocks over long timescales. The size of the thermally affected area depends on the duration of hydrothermal activity; the longer the system is active the larger is the thermal aureole around the fault. We used a numerical model of advective and conductive heat flow to calibrate the duration of hydrothermal activity using the AHe data. Combining low-temperature thermochronology with a thermal model can therefore be used as a tool to quantify hydrothermal activity over geological timescales.

INTRODUCTION

To gain deeper insights into the interaction of fluid flow and geological processes it is necessary to know the longevity of hydrothermal activity. However, to the present day it is difficult to determine the duration and age of hydrothermal flow events. Dating hydrothermal mineral deposits is often highly uncertain since accumulations of calcite and silica exhibit errors that may exceed the duration of short-term hydrothermal events. Such errors may be due to complex growth patterns and secondary mobility (Nuriel 2014). Furthermore, not all hydrothermal systems generate mineral deposits, making it even more difficult to date their existence. Low-temperature thermochronometers are not constrained to mineral deposits and can therefore serve as a tool for temporally constraining thermal processes in hydrothermal systems. With a closure temperature of as low as ~70°C, the (U-Th)/He thermochronometer is sensitive to thermal and tectonic processes in the upper crust (Reiners 2002). The upward flow of hot hydrothermal fluids through a fault causes temperature changes in the surrounding area. The longer a hydrothermal system is active, the more heat is transferred to the host rock. Low-temperature thermochronometers like the apatite (U-Th)/He (AHe) method, experience full or partial rejuvenation when exposed to elevated temperatures. The conducting heat from an active hydrothermal system can therefore reset or partially reset AHe ages in rocks adjacent to the heat source. The size of the area where rocks are affected increase with progressive hydrothermal activity. Consequently, it is possible to quantify the duration of hydrothermal activity if the reset of thermochronometers can be spatially distinguished.

First approaches to date hydrothermal activity using thermochronometers were made by systematically identifying limits of minimum and maximum flow time. The duration of a non-volcanic hydrothermal system in the Kii Peninsula (Southwest Japan) was quantified using zircon fission-track (ZFT) and apatite fission-track (AFT) data from host rock samples collected around hot springs using zircon and apatite fission track (Umeda et al. 2007). Zircon fission-track ages were consistent with the ages of non-altered rocks, indicating that surface temperatures of the hydrothermal system were below the zircon partial annealing zone. Apatite fission-track ages close to the heat source showed significantly younger ages than the ages of the non-altered host rocks collected away from the hot springs. Thus, altered samples have been reheated post-deposition to temperatures up to the AFT closure temperature. The authors were able to approximate the duration of non- volcanic hydrothermal activity of the Kii Peninsula by determining the beginning of it to be equivalent to the lowest AFT age. To identify the spatial and temporal patterns in hydrothermal flow associated with Au-deposits of the Carlin hydrothermal system Hickey & Tosdal (2012) and Hickey et al. (2014) mapped a thermal halo using AFT data. Thermal halos are associated with channelized fluid flow and provide a distal indicator for thermal conduction. The authors chose thermochronometers to be the preferred methodology because they do not only provide a sensitive temperature record but also a timeframe of thermal resetting. The width of thermal haloes is primarily a function of the flow duration, the temperature of the fluid and the magnitude of advective and conductive heat transfer. Of these factors, the duration of the hydrothermal events is the least well constrained (Hickey et al. 2009). Gorynski et al. (2014) quantitatively analyzed advective heat transport using AHe and Zircon-Helium (ZHe) thermochronology on samples from a borehole that was drilled into a normal fault in the southern Wassuk Range, Nevada, to link the timing, distribution and magnitude of fluid advection in the footwall to successive redistribution of heat by hydrothermal fluids into the hanging wall. To obtain information about paleo-depths and the local thermal evolution, Gorynski et al. (2014) additionally sampled the exhumed footwall block of the extensional-type geothermal system orthogonally to the normal fault. Their study revealed a geothermal anomaly represented by the partial retention zone (PRZ) that lead to the formation of a non-volcanic hydrothermal system in the hanging wall of the pull-apart structure.

Numerical models are needed to interpret thermochronological data and to describe the duration of hydrothermal fluid flow. In an earlier study by Leatherman (2010), sinter and vein deposits were studied to show that fluid flow in the Beowawe system occurred episodically over geological time scales. Concentration patterns of trace elements in sinter as well as differences of salinities in fluid inclusions are interpreted as evidence for episodic hydrothermal flow. Results of geochemical reaction path modeling suggest that fluid pathways must have shifted over time as fault permeability decreased due to mineralization. Hickey et al. (2014) introduced a model for a thermal history involving multiple episodes of hydrothermal fluid flow and heating, using apatite fission-track data of a gold deposit in Nevada. First, conductive heat flow into the stock was calculated using the numerical one-dimensional model code *Hefty v1.7.4* by Ketcham (2005). The results were then used to forward model the annealing of AFT. These model results were compared to AFT ages and track length data measured across the intrusion. Like Hickey et al. (2014), Gorynski et al. (2014) also used inverse and forward modeling to achieve time and temperature estimates for their samples but using (U-Th)/He dating instead. Because the thermal history of the foot wall was well-defined they were able to identify the duration and magnitude of juvenile reheating using the inverse model HeMP by Hager (2009). Forward modeling was done using Hefty. Model results were then compared to the AHe ages of the borehole samples.

A single-phase, single-pass hydrothermal model was used for the interpretation of the stable isotope data and present-day temperature in a recent study by Howald et al. (2015). Sinter deposit ages and isotopic composition data from ^{14}C in pollen and oxygen isotopes respectively delivered information about the Beowawe hydrothermal system over timescales of thousands of years. δ^{18}O values revealed an isotopic depletion of 20‰ over 5000-7000 years which can only be explained by a seismic induced increase in permeability. In their model, fault permeability is an important parameter and was used for model calibration to match heat-flow and temperature profiles. The authors found that the rate of conductive thermal recovery is much slower than the advective cooling.

Luijendijk (2012) discovered thermal anomalies in borehole samples in the Roer Valley Graben, which showed fission track ages that were too young to be explained by burial history or basal heat flow and inverted AFT-depth profiles. Luijendijk (2012) concluded that this anomaly can only be explained by a vertically confined heat flux and developed a numerical model of heat and fluid flow. He was able to show that the thermal overprint in AFT-ages were linked to a hydrothermal event 80Ma ago. This model was further developed by Luijendijk over the last years and the newest version is being used in this study.

With our research, we aim to develop a tool for determining the duration of hydrothermal systems on geological time scales, exceeding the time constraints achieved by prior studies. To attain this goal, we constrained the duration of an active hydrothermal system in Beowawe, Nevada, by combining high-resolution low-temperature thermochronological data from surface samples collected in the vicinity of this hydrothermal system with a new inverse thermal model (Luijendijk, unpublished). We analyzed apatite (U-Th)/He ages in 16 samples and obtained zircon U-Pb ages of the formation age of the volcanic host rock for four samples. We chose the Beowawe geothermal system because we can, unlike in active volcanic hydrothermal systems, directly distinguish conductive hydrothermal heating of a host rock by looking at the thermal overprint on thermochronometers. In volcanic hydrothermal systems the source of the heat that is conducted into the rocks surrounding a hydrothermal system is the magma chamber. A non-volcanic hydrothermal systems carries hot fluids from great depth to the surface so that the heat conducting into surface rocks comes from the thermal fluids themselves. A steep hillslope arising from the fault scarp enables for high resolution sampling. The volcanic host rock was likely to contain apatite and zircon crystals. Comparing thermally unaffected AHe ages to U-Pb ages in zircons permits an approximation of exhumation rates. The Beowawe hydrothermal flow regime and its sinter deposits are well studied. Modeling results can therefore be compared to existing estimates of flow duration by means of the sinter deposits. Dating this distinctive system gives an insight into the deep ground water flow and long-term hydrothermal history.

STUDY AREA

Tectonic setting

Subject for study is an active, non-volcanic hydrothermal system located near the town of Beowawe in north-central Nevada, USA (Figure 1). This unique geothermal area is situated in the Basin and Range province, which is an actively extending continental rift embedded within the North American western Cordillera (Parsons 1995). Tectonic extension started in mid-Tertiary times and is still active (White 1998). There are two distinct phases of structural development (Eaton 1982). Early extensional deformation began about 36 to 27 Ma ago. Characteristic for this early regime are normal faults with low dips and coeval volcanic rocks of calc-alkaline composition. The modern Basin and

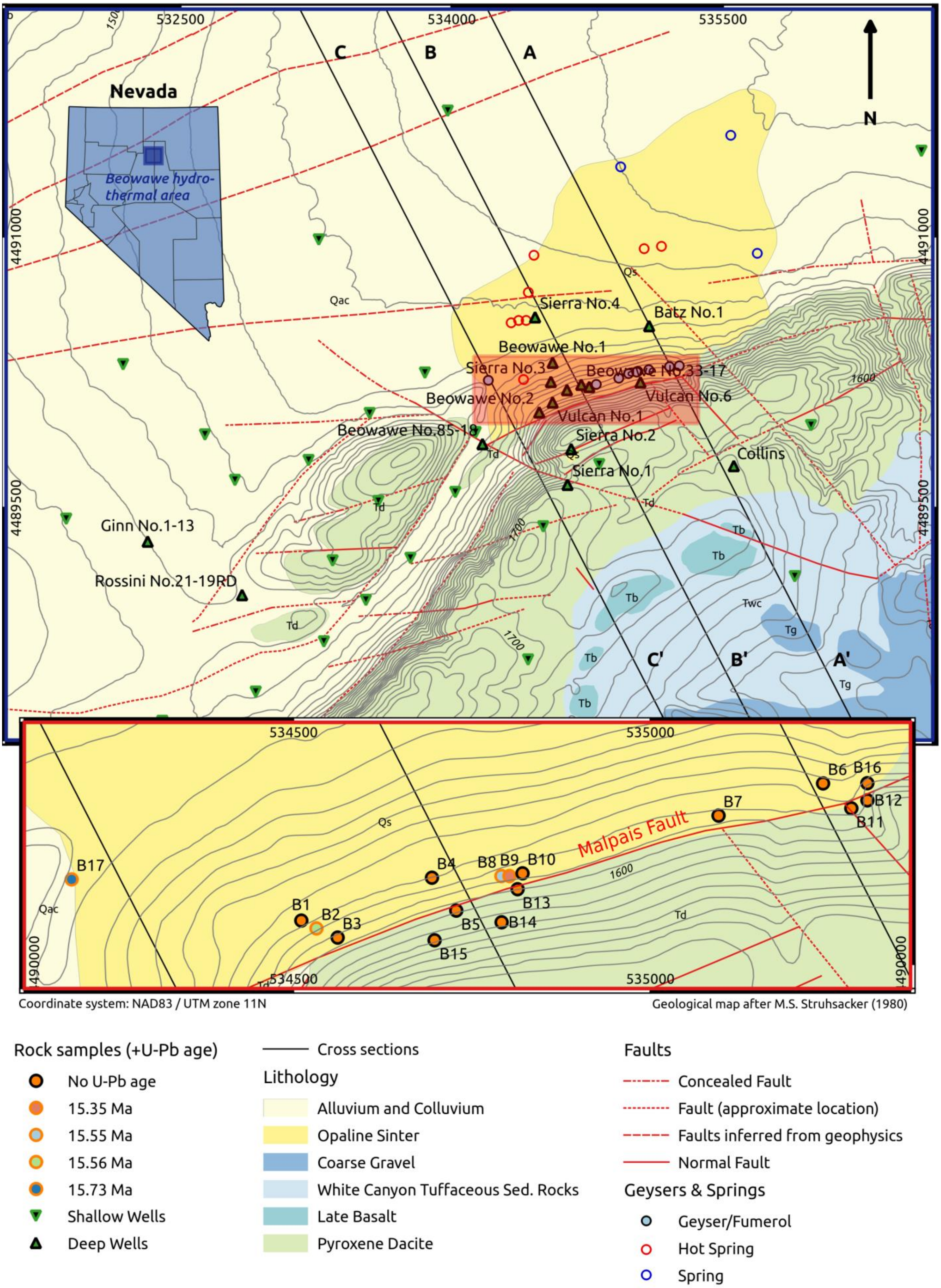

Coordinate system: NAD83 / UTM zone 11N

Geological map after M.S. Struhsacker (1980)

Figure 1 *Geological map of the Beowawe geothermal area. The map with a blue frame shows the local geological setting, locations of deep and shallow wells, as well as pre-developmental geysers and hot springs. The map with a red frame is a close-up of the hydrothermally active Malpais fault and shows the sample locations with their respective U-Pb age.*

Range structures evolved from mid-Eocene times until today. These structures are characterized by active block faulting with steep dips and relatively high structural relief. In-between the emplacement of calc-alkaline magma, episodic eruptions of basaltic lava flooded the province (Eaton 1982). The magmatic flux in the basin and Range province has been greatly reduced in the past 6Ma. Middle-Miocene volcanic activity led to the accumulation of dacite, basaltic andesite and basalt flow sequences that encompass most of the outcrops in the Beowawe hydrothermal area (Struhsacker 1980). What is unusual for this local setting is that there are no exposed volcanic rocks younger than 10 Ma (White 1998). Extensional-type geothermal systems achieve elevated temperatures by relying on deep circulation of water. High fluid temperatures are coupled with the presence of fault structures that provide pathways for the rapid upwelling of water and the high regional heat flow (Wisian et al. 1999). The Beowawe system is controlled by two intersecting major normal fault systems: The Dunphy Pass Fault zone and the Malpais Fault zone (Figure 1). Faulds et al. (2003) believe that a combination of west-northwest-directed extension in the east-northeast-trending Humboldt structural zone promote the deep circulation of fluids along the local faults including the Malpais fault zone. In addition, great fault and fracture density associated with en-echelon overlapping of normal faults enhance local permeability. The Beowawe hydrothermal system is confined by a northwest trending Oligocene to Miocene graben. Hot springs and geysers developed along the Malpais fault zone at the base of the inclined Malpais Rim. The extent of surficial hydrothermal activity in Beowawe is limited by northwest and west-north-west trending vertical faults that restrict the outflow of fluids along the Malpais scarp.

Stratigraphy and Lithology

The local geology of the study area is subdivided by a Paleozoic basement at depth that is unconformably overlain by Cenozoic volcanics and sediments. The basement is comprised of autochthoous carbonates that are in fault contact along the Devonian to Lower Missipian Roberts Mountain thrust with the allochtonous siliceous rocks of the Ordovician Valmy formation. Conglomerates of the Valmy formation are partially exposed at the Malpais Rim. Overlying the Valmy formation within the Basin and Range graben structure, there are Lower Miocene tuffaceous sediments with interbedded andesite flows and Ordovician clasts at the base of the Cenozoic section. These are capped by outcropping Middle Miocene basalt, dacite and basaltic andesite flows which vary in thickness due to the simultaneous development of a graben. In contrast to the normal regional thickness of less than 300 m, borehole data from the Beowawe exploration wells revealed a local thickness of up to 1200 m of Miocene volcanics above the old tuffaceous sediments (Zoback 1979; Struhsacker 1980). North-northwest striking Middle Miocene diabase dike swarms are located beneath the sinter terrace and cause a magnetic anomaly called the Idahoe-Nevada lineament (White 1998). A large, 65m thick Quaternary siliceous sinter terrace deposited by hot springs, fumaroles and geysers is located along the Malpais Rim tracing the graben bound Malpais fault zone (Rimstidt & Cole 1983).

Heat flow

Extension rates of 1.5 to 3 %/Ma for hot sub regions like the Battle Mountain High are a reason for anomalously high and variable heat flow in the Basin and Range rift system (Lachenbruch 1978). The Battle Mountain heat flow high covers a large area of northern Nevada, including the Beowawe hydrothermal system (Faulds et al. 2003). Here, deep circulating fluids reach high temperatures due to the local high heat flow, leading to hydrothermal activity. In the Basin and Range Province, high heat flow patterns result from a combination of (1) high background heat flow induced by the superposition of a Cenozoic thermal event and ongoing regional extension until the Quaternary, (2) high permeability in the upper crust due to extension, (3) a high regional heat flow and (4) contrasts in conductivity between ranges and valleys (Blackwell 1983). Local heat flow around the Beowawe sinter terrace is elevated to an average of 235mW/m² compared to a background heat flux of 118mW/m² which indicates that the Tertiary volcanic rocks act as a relatively impermeable cap forcing thermal waters to find permeable conduits for upward flow (Smith 1983).

Hydrogeology

Prior to 1959, the Beowawe hydrothermal area had the second greatest concentration of active geysers in the USA. Natural geysers, hot springs and fumaroles were located along the Malpais fault zone (White 1998). In the Beowawe system, hydrothermal fluids are transported to the surface by a steeply dipping normal fault. A large volume of sinter deposits gives information about the spatial distribution of past and present fluid flow. It also allows for broad estimations on the duration of hydrothermal activity. Olmsted & Rush (1987) calculated a total discharge rate of 0.018 m^3/sec based on a heat and fluid budget of the Beowawe geothermal area. The system is recharged by a deep groundwater aquifer. Low ^{3}He/^{4}He ratios are evidence for a non-volcanic heat source. The deficiency of mantle-^{3}He points towards a derivation of heat by thermal conduction through a thin crust (White 1998). The isotopic composition of modern Beowawe hydrothermal fluids plot near the meteoric water line (Howald et al. 2015).

Well tests indicate highly permeable zones located in the rock formations underneath the Malpais ridge and Wirlwind area (Zoback 1979). The hydrothermal reservoir is comprised of three storage layers that are characterized by high permeability: (1) a 6-7km deep zone of circulation within a carbonate aquifer beneath the Robert Mountain thrust , (2) an intermediate zone at depth of approximately 1km characterized by complex fault and fracture intersections and (3) a shallow zone at depth of about 200m within interbedded tuffaceous sections in a basaltic andesite layer in the uplifted footwall (Zoback 1979). Borehole measurements and chemical geo-thermometers show subsurface temperatures averaging 230°C at depth of >3km (Rimstidt & Cole 1983). Pre-developmental surface discharge temperatures were up to

95°C, which is the boiling temperature at the elevation of 1524m asl (Cole & Ravinsky 1984). Large flow capacities (permeability*reservoir interval thickness) of 60 to 240 md-m (6,32e-14 to 2,37e-13 m^3) made the Beowawe system prolific for commercial geothermal production (Epperson 1982). Geothermal exploration caused a decline in the local water table. As a result, all natural hot springs and geyser activity on the terrace ceased by September 1960 (White 1998).

Smith (1983) conducted a study on how cold, shallow ground water and thermal fluids affect each other by combining temperature data of the shallow subsurface with data of head distribution from piezometers. Temperature-depth profiles that are undisturbed by groundwater reveal a background gradient in the alluvium of 68°C/km leading to an estimated background heat flow of 118mW/m^2. Inflections characterized by a concave downward temperature-depth profile in the vicinity of the geysers and hot springs define a shallow thermal flow system where thermal waters flow from a deep reservoir into the cold ground water of the alluvium. Downward flow of cool groundwater can be identified by a concave upward temperature profile. After commissioning an electrical power plant, the two deep production wells tapping the Malpais fault zone cooled down and the brine chemistry became diluted in the following years. These changes indicate recharge of cold meteoric water into the geothermal system. (Benoit & Stock 1993). Olmsted et al. (1986) evaluated geologic, hydraulic-head, hydrochemical and temperature data from 24 shallow USGS test wells that show both a near-surface heat flow and a conductive anomaly. During this temperature survey, a confined zone of hydrothermal up-flow and lateral flow at shallow depth was identified. The authors conclude that these anomalies are caused by substantial lateral flow from the up-flow conduit system.

METHODS

Sampling and sample preparation

17 rock samples were collected along the Malpais fault in the vicinity of the Beowawe sinter terrace. All of them were taken at a different distance from the Malpais fault (Figure 1). The samples were crushed with a hammer and ground to a grain size of 250 µm using the Retsch BB-50 jaw crusher. The ground rocks were dried in the oven at 60°C and then sieved in fractions of >1mm, 500µm to 1mm, 250 to 500 µm and <250µm. The heavy minerals were pre-concentrated from the <250µm fraction using a Wilfley wet shaking table. Carbonates and Fe-oxy-hydroxides were dissolved in 5% acetic acid and grain aggregates were broken down in an ultrasonic bath. The samples were washed with acetone and dried at 60°C. Heavy and light minerals were further separated according to their densities using Lithium Polytungstate (LST) solution. The heavy minerals were separated into “ferric”, “magnetic” and “non-magnetic” fractions. Ferric minerals were removed with a hand magnet. Magnetic separation was done with a Frantz Magnetic Separator (Model L-1) at a side angle of 10°, a forward dip of 20° and a maximum electric current of 1.7 Ampere. Apatites and zircons were hand-picked under the Olympus SZX7 microscope.

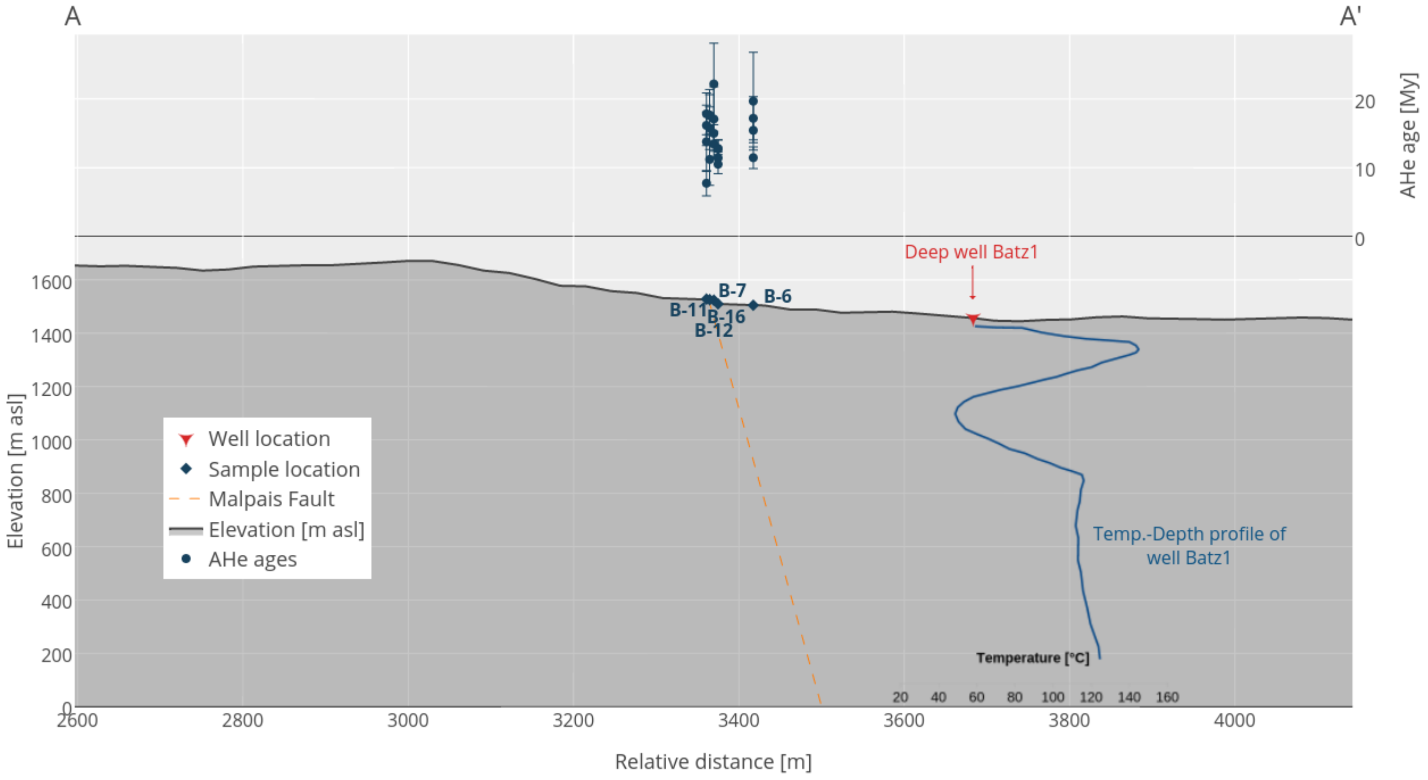

Figure 3 *In the upper panel, the measured AHe ages (dark blue circles with error bars) of the interpolated samples are plotted along profile A-A'. In the lower panel, the interpolated locations of the collected surface samples (dark blue rhombus) and the well locations (red),as well as the location of the Malpais Fault (orange dotted line) and the temperature depth profile of the Batz1 well (blue line) are correlated to the surface elevation along profile A-A'.*

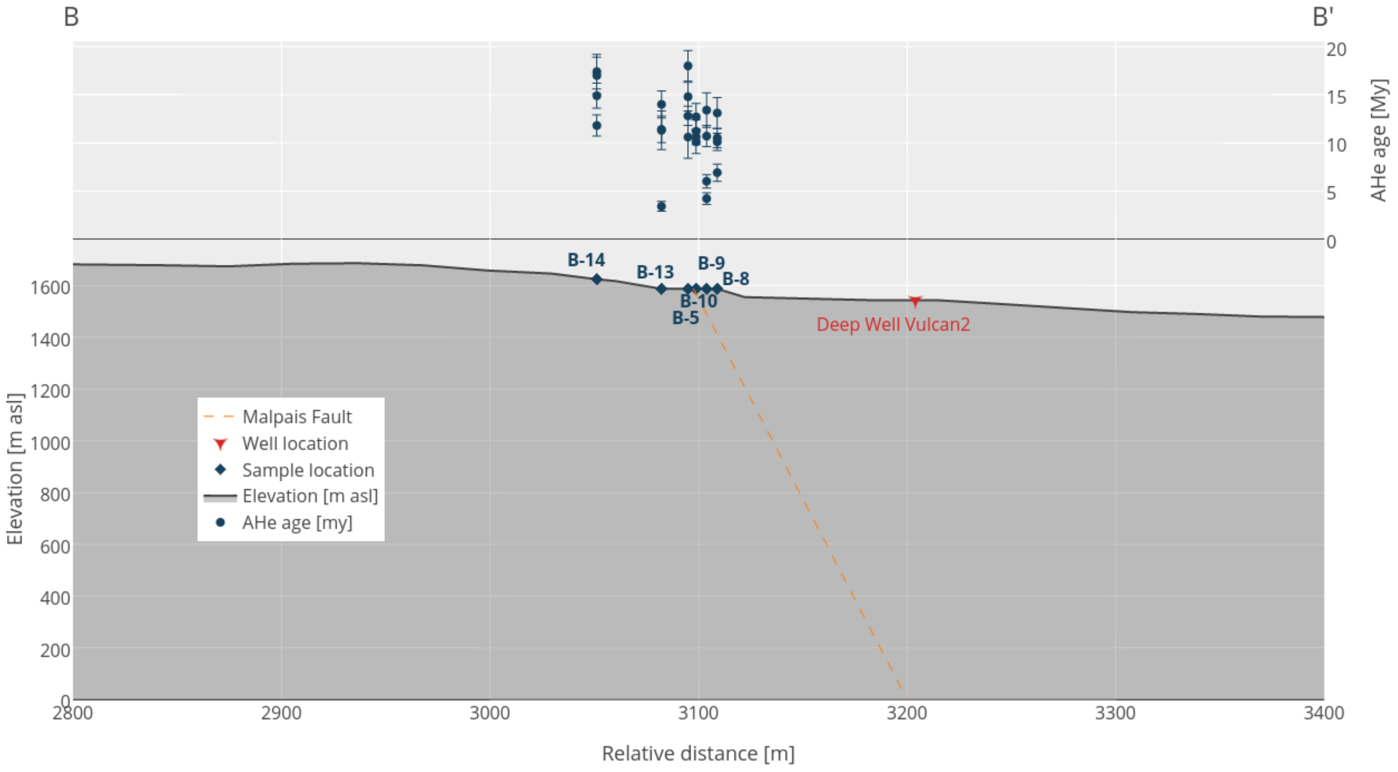

Figure 2 *In the upper panel, the measured AHe ages (dark blue circles with error bars) of the interpolated samples are plotted along profile B-B'. In the lower panel, the interpolated locations of the collected surface samples (dark blue rhombus, the well location of Vulcan2 (red) and the location of the Malpais Fault (orange dotted line) are correlated to the surface elevation along profile B-B'.*

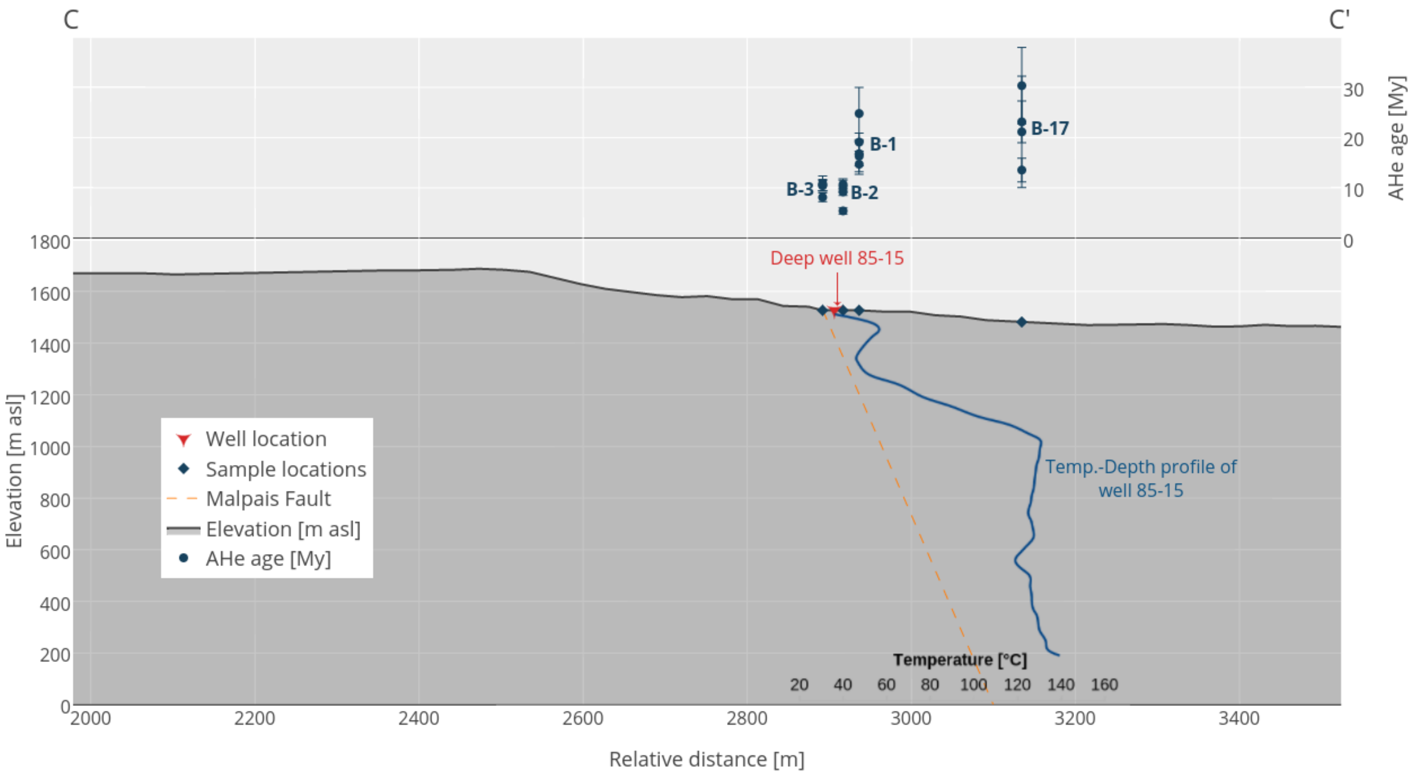

Figure 4 *In the upper panel, the measured AHe ages (dark blue circles with error bars) of the interpolated samples are plotted along profile C-C'. In the lower panel, the interpolated locationns of the collected surface samples (dark blue rhombus) and the well locations (red),as well as the location of the Malpais Fault (orange dotted line) and the temperature depth profile of the 85-18 well (blue line) are correlated to the surface elevation along profile C-C'.*

Quantitative sample analysis using XRD and Rietveld method

Table 1 XRD settings

Anode material of x-ray tube	Copper (Cu)
Voltage	40 kV
Current	30 mA
Mask	17.20 mm
Divergent slit angle	0.5°
Distance of divergent slit to sample	140 mm
Anti-scatter slit angle	0.5°
Height of receiving slit	0.2 mm
Scan range	4.0° – 69.5°
Step size	0.02°
Counting time	10 sec

To determine the rock composition and look for secondary minerals we conducted x-ray diffraction (XRD) on five samples (B-4, B-5, B-8, B-9, B-14) using a Philips X'Pert MPD and a PW 3050/10 goniometer. The sieved sample fraction <250µm was mixed with the internal standard zinc oxide (ZnO) at a ratio of 8/2 respectively. The mixture was then back loaded on a powder mount with a diameter of 27mm. Measurement settings are summed up in the table below (Table 1). The diffractogram was analyzed qualitatively using the software X'pert High Score by PANAlytical. Qualitative analysis was performed by Volker Karius of the department of sedimentology at the University of Göttingen with the Rietveld method (Young 1995).

Zircon U-Pb geochronology

U and Th are accessory elements in zircon minerals, but Pb is not. The Pb within a zircon crystal is radiogenic and the result of the decay of radioactive U. The ratio of U and Pb isotopes gives information about the crystallization age of a rock. This method is not sensitive to temperatures in the upper crust (Paces & Miller 1993; Frei & Gerdes 2009).

The zircon crystals from four samples (B-2, B-8, B-9 and B-17) were hand-picked under the microscope. Further laboratory proceedings and the following methodical description were provided by István Dunkl of the Göttingen Geochronology Lab: “The selected crystals were fixed on a double-side adhesive tape attached to a thick glass plate and embedded in a 25 mm diameter epoxy mount. The crystal mounts were lapped by 2500 mesh SiC paper and polished by 9, 3 and 1 micron diamond suspensions. For all zircon samples and standards used in this study cathodoluminescence (CL) images were obtained using a JEOL JXA 8900 electron microprobe at the Geozentrum Göttingen in order to study their internal structure and to select homogeneous parts for the in-situ age determinations. The carbon coating used for CL imaging was later removed with a brief hand polish on a 1 micron diamond cloth. The mounts were cleaned in different steps with diluted HCl, ethanol and deionised water in an ultrasonic bath to remove surface lead contamination before introduction into the sample cell.

The in-situ U-Pb dating was performed by laser-ablation single-collector sector-field inductively coupled plasma mass spectrometry (LA-SF-ICP-MS). The method employed for analysis is described in detail by (Frei & Gerdes 2009). A Thermo Finnigan Element 2 mass spectrometer coupled to a Resonetics Excimer laser ablation system was used. All age data presented here were obtained by single spot analyses with a laser beam diameter of 33 µm and a crater depth of approximately 10 µm. The laser was fired at a repetition rate of 5 Hz and at nominal laser energy output of 25 %. Two laser pulses were used for pre-ablation. The carrier gas was He and Ar. Analytes of ^{238}U, ^{235}U, ^{232}Th, ^{208}Pb, ^{207}Pb, ^{206}Pb, mass204 and ^{202}Hg were measured by the ICP-MS. The data reduction is based on the processing of ca. 50 selected time slices (corresponding ca. 14 seconds) starting ca. 3 sec. after the beginning of the signal. If the ablation hit zones or inclusions with highly variable actinide concentrations or isotope ratios then the integration interval was slightly resized or the analysis was discarded (~1% of the spots). The individual time slices were tested for possible outliers by an iterative Grubbs test (applied at P=5% level). This test filtered out only the extremely biased time slices, and in this way usually less than 2% of the time slices were rejected. The age calculation and quality control are based on the drift- and fractionation correction by standard-sample bracketing using GJ-1 zircon reference material (Jackson et al. 2004). For further control the Plešovice zircon (Sláma et al. 2008), the 91500 zircon (Wiedenbeck et al. 1995) and the FC-1 zircon (Paces & Miller 1993) were analyzed as "secondary standards". The age results of the standards were consistently within 2σ of the published ID-TIMS values. Drift- and fractionation corrections and data reductions were performed by our in-house software (UranOS; Dunkl et al. 2008). The level of Hg-corrected ^{204}Pb signal was very low, thus no common lead correction was required. The number of single-grain ages per sample ranges between 20 and 47."

Apatite (U-Th)/He thermochronolgy

(U-Th)/He thermochronology is to date the most temperature sensitive geochronological dating method. The method is based on the production of ^{4}He as a result of the radioactive α-decay of uranium and thorium isotopes in accessory minerals such as apatite, zircon or titanite. Despite the long half-life, six to eight α-particles per parent nuclei are ejected, leading to the relatively fast accumulation of ^{4}He (Reiners 2002). Depending on the temperature, the He either diffuses out of the crystal (above 85°C) or is being retained (below 40°C). Ranging between 40°C and 85°C, He retention is very temperature sensitive (Wolf et al. 1998). This temperature range is also referred to as the partial retention zone. The helium retained in an apatite is additionally dependent on crystal size and cooling rate. Larger crystals retain larger fractions of ^{4}He. Small crystals lose a larger fraction of ^{4}He due to long α stopping distances. Slow cooling rates and long residence times in the partial retention zone lead to a larger He loss. Thus, corrections and modeling have to be applied to the raw (U-Th)/He data (Reiners & Farley 2001; Wolf et al. 1998; Farley et al. 1996).

Apatite crystals were hand-picked under a binocular microscope. Selected crystals had a minimum width of 60 µm, euhedral shape and equal widths in all directions perpendicular to the c-axis. To secure intact shape and exclude minerals with inclusions and cracks, further selection was done using a polarizing microscope. Four apatite crystals per sample were analyzed. Sample B-4 did not contain any apatite crystals. The mineral grains were enclosed in a pre-cleaned platinum capsule of ~1x1 mm size. Further laboratory proceedings and the following methodical description were provided by István Dunkl of the Göttingen Geochronology Lab: "The Pt capsules were heated in the full-metal extraction line by an infra-red laser for 2 minutes in high vacuum. The extracted gas was purified using a SAES Ti-Zr getter while being kept at 450 °C. The chemically inert noble gases and a minor amount of other rest gases were then expanded into a Hiden triple-filter quadrupole mass spectrometer equipped with a positive ion counting detector. Beyond the detection of helium the partial pressures of some rest gases were continuously monitored (H_2, CH_4, H_2O, N_2, Ar and CO_2). The blanks were estimated using the same procedure on empty Pt tubes (max. 0.0003 and 0.0008 ncc ^{4}He; cold and hot blanks, respectively). Crystals were checked for degassing of He by sequential reheating and He measurement. The amount of He extracted in the second runs are usually below 1% in case of apatites. The analysis procedure was operated by HeLID automation software through a K8000/Poirot interface board (developed by I. Dunkl, Göttingen). The He signal was processed and evaluated by the factory-made software of the mass spectrometer (MASsoft, HIDEN). During standard and sample measurements 240 readings of the mass spectrometer were recorded.

Following degassing, samples were retrieved from the gas extraction line, spiked with calibrated ^{230}Th and ^{233}U solutions. The apatite crystals were dissolved in a 4% HNO_3 + 0.05% HF acid mixture in Savillex teflon vials. Each sample batch was prepared with a series of procedural blanks and spiked normals to check the purity and calibration of the reagents and spikes. Spiked solutions were analyzed as 0.4 ml solutions by isotope dilution on a Perkin Elmer Elan DRC II ICP-MS and Thermo iCAP Q mass spectrometers with an APEX micro-flow nebulizer. Procedural U and Th blanks by this method are usually very stable in a measurement session and below 1.5 pg. Sm, Pt and Ca were determined by external calibration. The oxide formation rate and the PtAr - U interference was always monitored, but the effects of these isobaric argides were negligible relative to the signal of actinides. The data of the ICP-MS measurements were processed by an in-house freeware software (PEPITA, url: www.sediment.uni-goettingen.de/staff/dunkl/software). Usually 40 to 70 readings were considered, and the individual outliers (spikes) of the $^{233}U/^{238}U$ and $^{230}Th/^{233}Th$ ratios were tested and rejected according to the 2 s.d. criterion. The ejection correction factors (F_t) were determined for the single crystals by István Dunkl, who uses an in-house spread sheet with a modified algorithm of Farley et al. (1996). The (U-Th-Sm)/He ages were calculated by the Taylor Expansion Method (after Des Patterson). The Sm content was also considered for age calculation."

Determination of internal zoning of actinides in the apatite crystals

Zonation of U and Th would affect the (U-Th)/He age due to over or under correction of alpha ejection, i.e. the ejection of He out of the rim zones of the crystal. To perform α-ejection correction (F_T correction) of the (U-Th)/He ages in the apatite crystals, the spatial extent of zonation was determined on six samples. In a first attempt, this was done by fission track analysis. Apatite crystals from six samples (B-2, B-5, B-7, B-8, B-9, B-13) were embedded in epoxy, polished and etched for at first 20 sec. and again for 5 sec. in 5.5N HNO_3 acid. Fission tracks were observed under a petrographic microscope. Because the fission track density was too low (mostly <10 tracks per crystal) no characteristic pattern could be detected in the studied samples. Then, laser ablation was performed along lines in order to detect the actinide concentration profiles across apatite crystals. For that, four well developed half-polished apatite crystals of each sample were selected and laser ablation profiling perpendicular to the c-axis was performed. Laser ablation cross profiling was performed with a 10 micron beam diameter, and a speed of 3 microns/sec. Only the Pb, Th and U isotopes were detected.

Thermal model

We used a new inverse 2D thermal model code, beo.py (unpublished, author: Dr. Elco Luijendijk), to simulate the temperature history of the rocks surrounding a hydrothermal system (Figure 5). The model code simulates advective and conductive heat transfer and uses the modeled temperature history to model apatite (U-Th)/He ages of synthetic rocks samples. The temperature history of rocks is calculated by solving the advective-conductive heat flow equation:

$$\rho_b c_b \frac{\partial T}{\partial t} = \nabla K \nabla T - \rho_f c_f \vec{q} \nabla T \tag{1}$$

where $\rho_{b,f}$ is bulk and fluid density [kg m^{-3}] respectively, $c_{b,f}$ is the specific heat capacity [J K^{-1} kg^{-1}] of the rock or fluid respectively, K is the hydraulic conductivity [W m^{-1} K^{-1}], T is temperature [K] and q is fluid flux [m s^{-1}]. The left hand side of the heat flow equation is the change of temperature over time, the first term on the right hand side is conductive heat flow and the second term is advection by fluid flow (q). The heat flow equation (1) is reorganized into an implicit form and solved using the generic finite element model code Escript (Gross et al. 2007; Poulet et al. 2012; Schaa et al. 2016).

According to Luijendijk (unpublished), this is a relatively simple setup that is computationally efficient and allows for a large number of parameter combinations to be explored, contrasting fully coupled fluid and heat flow models of hydrothermal systems (see e.g. (Howald et al. 2010)), where the fluid flux is modeled directly as a function of driving forces and permeability.

The fluid flux term (q) is a fixed value in a single fault zone and two horizontal aquifers connected to this fault. A fixed temperature is assigned to the lower model boundary according to the regional geothermal gradient. No heat flow is allowed over the left and right hand model boundary. To ensure realistic land surface temperatures the upper model boundary consists of a layer of 40 m of air overlying the land surface. This layer of air is assigned a specified temperature that corresponds to the average annual air temperature of 10 ˚C. Heat transfer between the surface and the atmosphere is modeled as a conductive heat flow. An artificially high value of thermal conduction of the air layer is used to account for the relatively efficient heat transfer by turbulence and latent heat flow above the land surface. Values for thermal conductivity of air are based on literature values of sensible heat flux. Sensible heat flux H [W m^{-2}] at the land surface is given by:

$$H = \frac{\rho c}{ra(T_a - T_s)} \tag{2}$$

where ρ is density [kg m^{-3}], c is the specific heat of air [J kg^{-1} K^{-1}], ra is the aerodynamic resistance [s m^{-1}], T_a is the air temperature at a reference level and T_s is the surface temperature (Bateni & Entekhabi 2012). Rewriting this to the conductive heat flow equation gives a value for the effective thermal conductivity [K_s] between the surface and the reference level z:

$$K_s = \frac{\rho c}{ra * \Delta z} \tag{3}$$

where Δz is the difference between the surface and the reference level [m] (Luijendijk, unpublished). For our model simulations we represent heat flow in the air layer above the surface using an effective thermal conductivity of 50 W m^{-1} K^{-1}.

The initial temperature in the subsurface is being modeled by solving eq. 1 for a steady-state situation (ie. dT/dt = 0). Subsequently, fluid fluxes are added to the fault zone. Equation 1 is then used to model the transient response of the system to the upward fluid flux along the fault. (Luijendijk, unpublished)

The modeled temperature history is used to calculate AHe ages for rocks located at the land surface. Helium production and diffusion in apatites and (U-Th)/He ages are calculated using the Eigenmode method with the modeled temperature history as the input (Meesters & Dunai 2002a; Meesters & Dunai 2002b). The diffusivity of helium in apatites is dependent on the radiation damage and is calculated using the RDAAM model by Flowers et al. (2009). Modeled AHe ages are then compared to the observed AHe ages of the rock samples. Exhumation is taken into account by lowering the land surface stepwise, with steps of 0.5 m.

In addition to modeling the AHe-age over time, the model code can also simulate downhole temperature curves in deep wells (Figure 5). Downhole temperatures can be determined along a vertical profile in the rock layer of the model domain.

In this study, the thermal history was calculated for three cross-sections perpendicular to the Malpais fault (A-A’, B-B’ and C-C’, Figures 2, 3 and 4). Samples and wells closest to either cross section were interpolated onto the profile. Pre-existing borehole data was used to produce temperature-depth profiles and lithology logs. Profile length and width of the model domain is determined to be 8000m. The rock layer in the model domain is cut by a normal fault. Depending on the profile, the rock layer consists of different lithologies that show an offset between the hanging wall and the foot wall of the Malpais fault. To ensure numerical stability we used a finer grid along the fault. In general, the model runs more stable, the smaller the cell size becomes. Good values for grid sizes were tested to be 100m for the general cell size, 5m for the cell size in the air layer, 5m within the fault damage zone and 500m at the model base.

The specific fixed parameters for the thermal model were taken from previous studies on the Beowawe system. Caskey and Wesnousk (2000), amongst others, studied the distribution and recency of active fault movement in the Beowawe geothermal production field. They were able to determine that there was little uplift in the graben system in recent times. Zoback (1979) determined the total vertical offset of the Maplais fault to be increasing from NE to SW, with a displacement of 225 m in the vicinity of the Batz1 deep well and a displacement of 380m at the vicinity of the Ginn well (see map in Figure1). These deep wells drilled by Chevron also reveal a general fault rake of 65°. Bulk thermal conductivities of volcanic and intrusive rocks were determined at 2W$m^{-1}$$K^{-1}$ with exceptions of significantly lower conductivities for dacite flows and tuffaceous sediments (Smith 1983).

To calibrate subsurface fluid fluxes, present-day temperatures are modeled and compared with borehole temperatures recorded by Middleton (1961) and Iovenitti &

Epperson, Jr. (1981). For AHe age modeling, an average of the crystal size and U/Th content was calculated for the analyzed apatite crystals of each cross section. Table 2 summarizes the fixed parameters that were used for the modeling in this study.

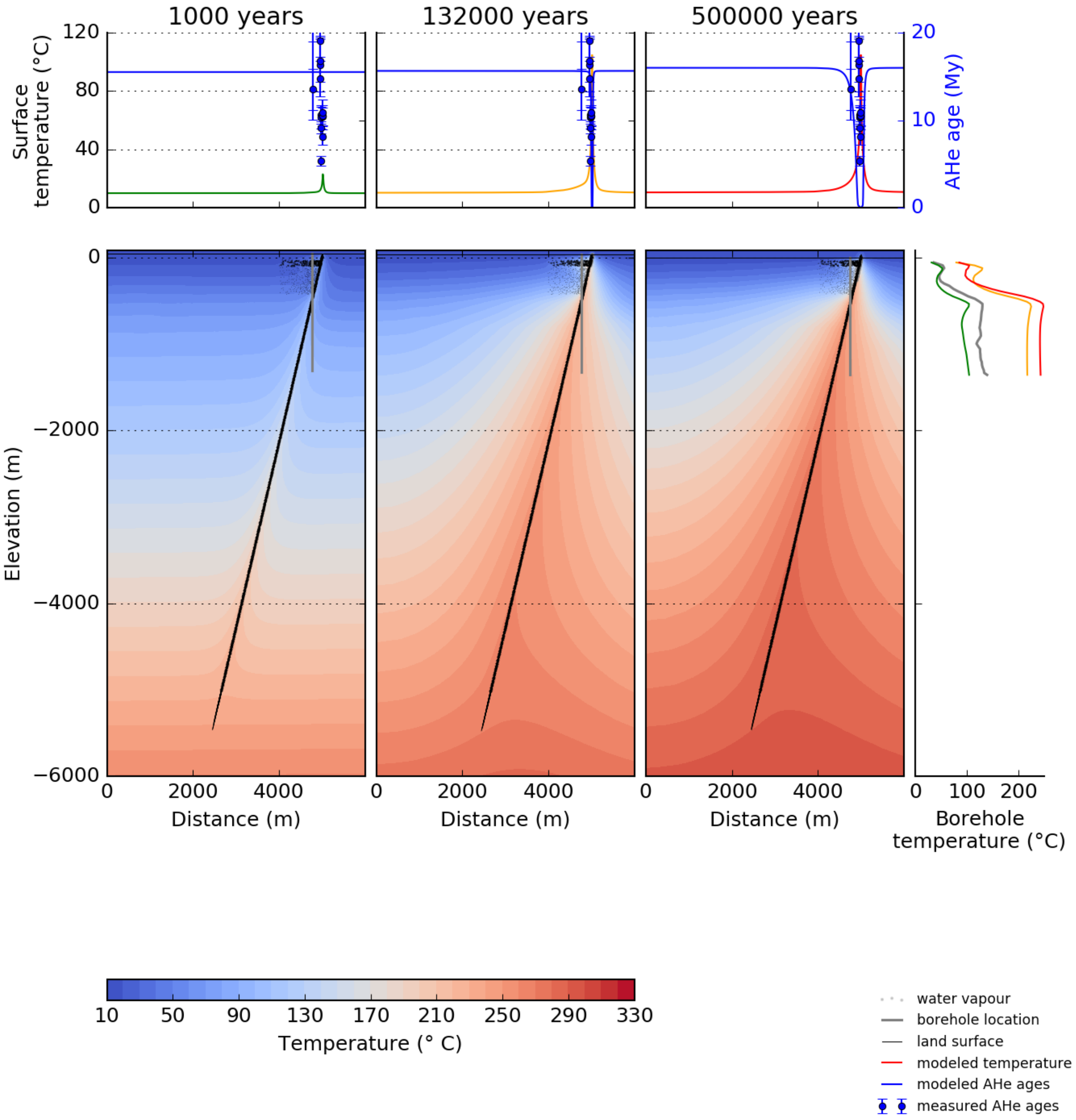

Figure 5 *Schematics of the model output. The upper panel shows the temperature (green, yellow and red lines) as well as the modeled AHe age (blue line) over distance. Each panel represent the situation after a certain time of hydrothermal activity (label above the respective panel). Measured AHe ages of the crystals are shown (blue circles with error bars) at the distance of the respective sample to the normal fault. The corresponding figures underneath the upper panels visualize the subsurface temperature at depth and over distance. The normal fault is shown in black. Arrows mark the fluid flow directions in the fault and in aquifers. The magnitude of a fluid flux is visualized by thinner arrows for low fluid fluxes and thicker arrows for high fluid fluxes. The lower right panel shows the measured temperature-depth profile of a deep well (grey line) in comparison to modeled temperature-depth profiles (green, yellow and red lines) at the same running time as the upper panels and their corresponding depth-distance profiles.*

Table 2 *Fixed model parameters*

Parameter	Value	Unit	Source
Width of model dimension	8000	m	
Total depth of model dimension	8000	m	
Air hight (model dimension)	40	m	
Cell size	100	m	
Cell size air	5	m	
Cell size fault	5	m	
Cell size base	500	m	
Size of timestep	250	yr	
Partial reset limit	0.75		
Reset limit	0.1		
Effective thermal conductivity	50	W m-1 K-1	
Air temperature	10	°C	Olmsted & Rush (1987)
Crystallization age	15.6	Myr	
Stopping distance of alpha particle	2.10E-05	m	Ketcham et al. (2011)
Fault angle	65	°	Zoback (1979), Struhsacker (1980)
Fault bottom	-5000	m	Howald et al. (2015)
Displacement at Batz1 well		m	
Displacement at Beowawe 85-18 well		m	
Thermal conductivity alluvium	1.68	W m-1 K-1	Smith (1983)
Thermal conductivity coarse gravel	1.6	W m-1 K-1	
Thermal conductivity basalt	1.6	W m-1 K-1	
Thermal conductivity basaltic andesite	2.26	W m-1 K-1	
Thermal conductivity tuff	1.58	W m-1 K-1	
Thermal conductivity valmy formation	4.44	W m-1 K-1	
Porosity alluvium	0.3		http://web.ead.anl.gov/resrad/datacoll/porosity.htm
Porosity coarse gravel	0.21		
Porosity basalt	0.17		
Porosity basaltic andesite	0.05		
Porosity tuff	0.25		
Porosity valmy formation	0.08		

Temperature data

Temperature data from hydrothermal exploration programs between the 1960ies and 1980ies were gathered and digitized (Figure 6). A final report prepared for the U.S. department of Energy by J.L.Iovenitti and I.J. Epperson, Jr. (1981) who performed their work under a contract with Chevron Resource Company documented and evaluated the Beowawe geothermal area evaluation program. The report summarizes several exploration programs, including shallow temperature hole data, a mercury soils sampling survey, a self-potential survey, the documentation of drilling the 5929-foot deep Beowawe 85-18 exploratory well and running geophysical logs in the bore hole. We were mainly interested in the temperature-depth profile of the deep well Beowawe 85-18. The well was drilled and completed from Feburary 22nd, 1980, to June 2nd, 1980. Temperature-depth profiles were conducted in 5 separate runs on May 10th and 11th 1980. The only well in the vicinity of profile B-B' that we were able to find data on is Vulcan2. This well was static, having been closed on January 8th, 1962. Temperature-depth measurements were done on March 30th and 31st in 1962. Besides the fact that the author W.M.Middelton (1961) of Magma Power Co. reports that the well of Vulcan2 was in "extremely bad" condition at the time of the survey and that the thermometer plum got stuck several times in "the crookedest hole they have encountered", the temperature data is not usable for our modeling purposes. The depth of the well is with its 200m depth not deep enough to reflect the background thermal gradient. The borehole was reportedly clogged by mineral deposits. Numerous fumaroles and vents were discharging considerable volumes of steam in the immediate vicinity, interfering with the well. The temperature survey reported very high borehole temperatures of 180°C at the surface level, rising to 193°C at a depth of 180m. Because this temperature survey is not usable for this study, we decided not to model the temperature-depth profile for profile B-B'. Unfortunately there was no public report available on well Batz1. A temperature-depth profile was digitized after a chart in the study by Garg et al. (2007). The date of the completion of well construction and the date of the temperature survey are unknown.

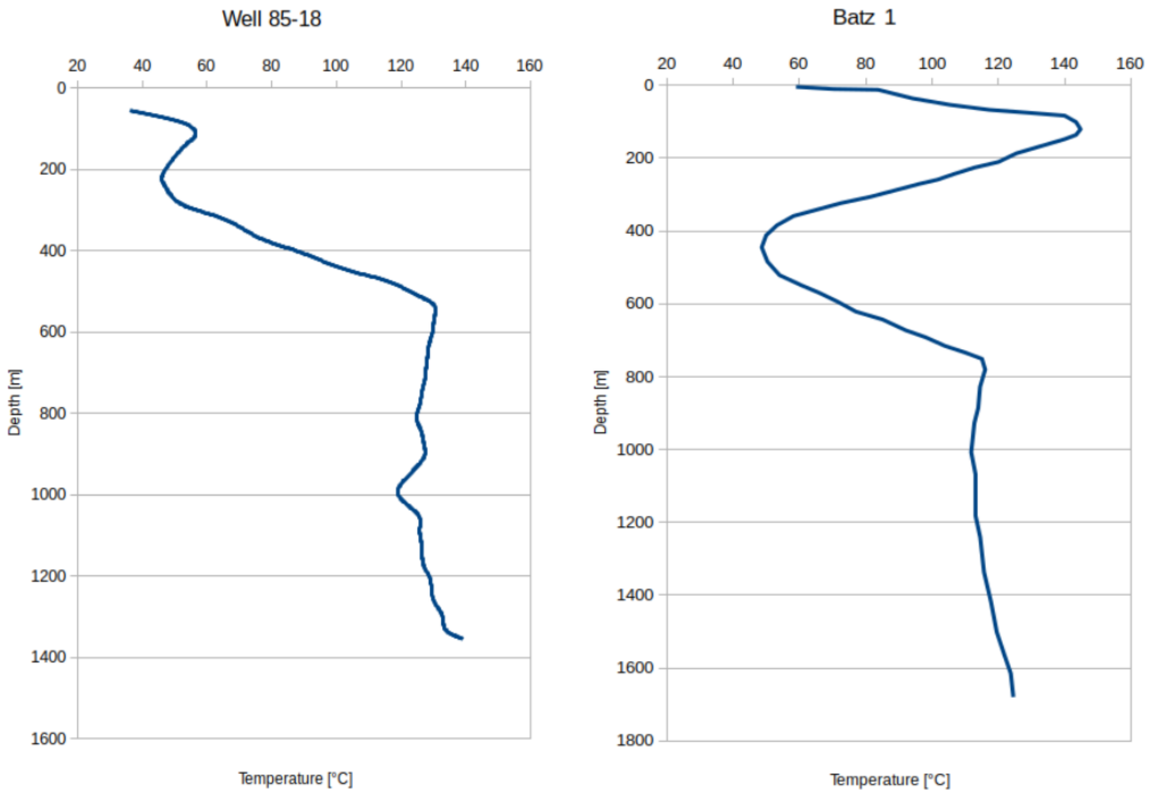

Figure 6 *Temperature-depth profiles of well Beowawe 85-18 (left) from Iovenitti & Epperson, Jr. (1981) and Batz1 (right) from Garg et al. (2007).*

Sensitivity analysis

A sensitivity analysis was performed to test the influence of model parameters on the thermal overprint of AHe data in surface samples adjacent to the hydrothermally active Malpais fault. The parameters and their range are listed in Table 3. A first model run was performed with the initial base values that were taken from earlier studies on the Beowawe hydrothermal system (see “value” in Table 3). For each parameter listed in Table 3, a range of values were tested by changing the respective parameter in each model run while keeping all other parameters fixed to their initial base values. Completely fixed parameters are listed in Table 2.

For model simulations using Luijendijk’s (unpublished) code, the width of the fault damage zone is controlling fault permeability and fluid flux. No direct measurements of the Malpais damage zone width were performed. However, studies on fault zone architecture show that there is a positive correlation between fault damage zone (or fault thickness) and displacement (Bense et al. 2013; Childs et al. 2009; Caine et al. 1996). Based on these studies we derived an estimate of the fault damage zone for the Malpais fault. With a displacement of ~200m and a crystalline bed rock we used fault zone thickness values varying between 10 and 30m for our parameter range (see “range” in Table 3).

On the basis of Howald et al.'s (2015) modeling, we decided on a background geothermal gradient of 0.04°C m^{-1}. This is in accordance with Zoback's (1979) and others reported reservoir temperature of 210-230°C. The deep reservoir is located in a carbonate layer of the Valmy formation at depth of ~5km. Smith (1983) reports a general background heat flow of 110mW m^{-2} in this part of the Battle Mountain heat flow high. With thermal conductivities varying between 1.6 and 4.4W $m^{-1}K^{-1}$ for the different lithologies, the geothermal gradient could vary between 0.068 and 0.025 K m^{-1}.

Sample B-14 is located at the uplifted foot wall block of the normal fault and has an AHe age equal to the U-Pb age of ~15.6Ma. It has not been exposed to temperatures above 70°C since the last 15Ma. With an average surface temperature of 10°C, the maximum temperature difference this sample has been exposed to is 60°C. With a geotherm of 40°C km^{-1}, the absolute maximum of exhumation could have been 1500m/15Ma. This leads to an upper limit for the exhumation rate of 1e-4m yr^{-1}. However, there is only ~100m of sediment fill inside the graben. If that is assumed to equal erosion it would lead to an exhumation rate of 6.7e-6m yr^{-1} for the lower limit. In their paper on “Post-tectonic landscape evolution of a coupled basin and range”, Jungers & Heimsath (2016) determined the erosion rate in SE-Arizona to be between 30 and 60 m/Ma. The study area is located in the Basin and Range as well and is exposed to a similar climate as Beowawe is. Their results are within the exhumation limits of the Malpais fault system. In the model code exhumation is equal to erosion. In a general study on accelerated mountain erosion under a cooling climate Herman et al. (2013) reported upper erosion levels of 1e-2m yr^{-1} and lower erosion limits of 1e-5m yr^{-1} for the last 8Ma. Supported by these estimates, we tested exhumation rates ranging between 1e-5 and 1e-3m yr^{-1} in our sensitivity analysis.

Based on a detailed study on the hydrogeology of the Beowawe geothermal system by Olmsted & Rush (1987) and other studies by e.g. Howald et al. (2015) and White (1998), the pre-developmental discharge rate at the Beowawe hydrothermal system was estimated to have been ~400m²/sec. This value is based on recent hydrogeological activity. However, this value may have changed over geological timescales. Nolan & Anderson (1934) reported that hydrothermal discharge varied seasonally. Both Howald et al. 2015 and Banerjee et al. (2011) suggest a transient and episodic fluid flow for the Beowawe system. For all these reasons, it is important to keep in mind that fluid flux possibly has changed over geologic time scales. It is therefore an important parameter to test in our modelling. For the sensitivity analysis we tested values ranging between 100 and 600 m²/sec.

Table 3 *Fitted model parameters*

Parameter	Value	Range	Unit	Source
Exhumation rate	0.0001	1e-4 – 3e-5	m/yr	Jungers and Heimsath (2015)
Thermal gradient	0.04	0.02- 0.06	C°/m	Howald et al. (2015), Zoback (1979)
Fault width	10	10 – 30	m	Caine (1996), Bense (2013)
Fault flux	400	150 – 500	m²/sec	Ohlmsted and Rush (1987)
Total depth (model dimension)	6000	6000-10000	m	

RESULTS AND DISCUSSION

Mineralogy of the studied samples

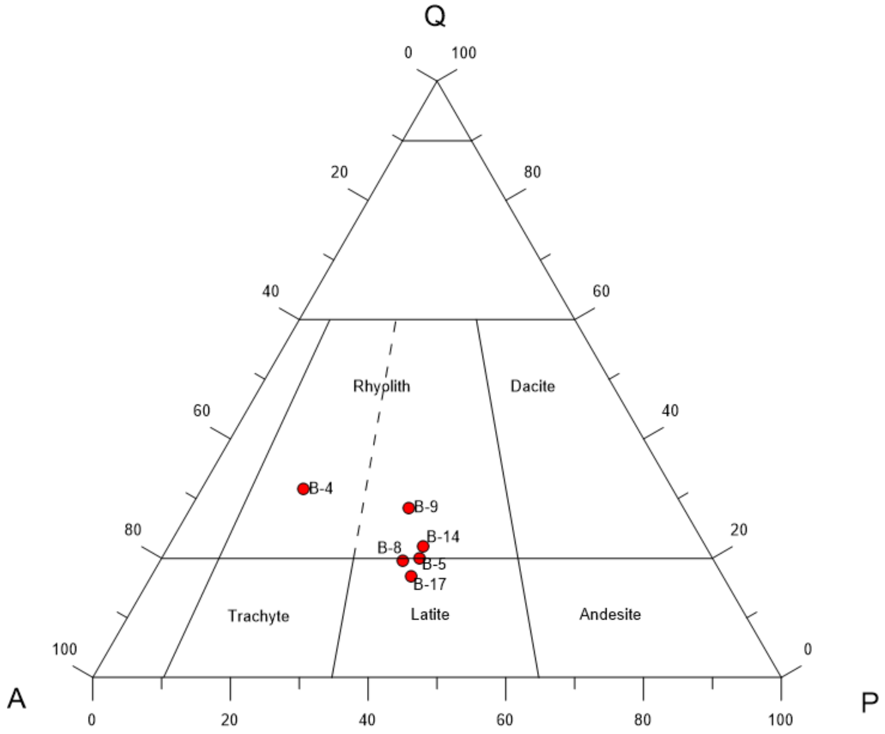

Figure 7 *Streckeisen diagram showing the total weight percentage of all quartz, potassium feldspar and plagioclase mineral phases in the analyzed samples.*

The crystal phases of all six samples were determined using the Rietveld method (after Young (1995)). The total weight percentage of all quartz, potassium feldspar and plagioclase mineral phases were added up respectively and normalized to 100%. Results were plotted into a Streckeisen diagram (Figure 7). Contradicting the geological map of Stuhsacker, the majority of samples plotted into the lower ryolith field of the Streckeisen diagram. Sample B-17 contains less Quartz than most other samples and plots into the latite field.

U-Pb geochronology

The analyzed zircon crystals showed rather high U concentration. Thus, the young ages could be measured at high precision. The average U-Pb age, which represents the crystallization age of the volcanic rocks, was determined to be 15.6 Ma (Table 4). Sample 17 contains much more U and Th than the other three samples. All four samples had a very small error of max. +/- 0.11 Ma years. The concordia plots (Appendix pages xi and xii.) were constructed by the help of Isoplot/Ex 3.0 (Ludwig 2012).

Table 4 *Results of U-Pb analysis of the Göttingen Geochronology laboratory. Ages are shown in Ma including their decay constant errors. For samples B-2, B-8 and B-9 a total of 15 crystals were analyzed. 17 samples were analyzed for sample B-17.*

Sample	Dated crystals	Considered data	Concordia age [Ma]	Uncert. [Ma]	MSWD	Probability	Uranium [µg/g]	Thorium [µg/g]	Log alpha density	Corrected Age [Ma]	Uncert. [Ma]
B-2	15	13	15.25	0.11	0.07	0.79	1358	1985	16.9	15.6	0.3
B-8	15	14	15.23	0.10	0.18	0.68	1283	1329	16.9	15.6	0.3
B-9	15	15	15.02	0.11	2.80	0.10	1253	1057	16.9	15.4	0.3
B-17	17	17	15.47	0.05	0.01	0.91	1959	3231	17.1	15.7	0.3

(U-Th)/He data

Table 5 summarizes the results of (U-Th)/He analysis. The map in Figure 8 shows the surface samples along the Malpais fault with its average AHe ages. The unweighted average age of six samples (B-1, B-6, B-7, B-14, B-16, B-17) show AHe ages similar to the U-Pb age of the host rock. These samples were thermally unaffected since their crystallization. Most of them are located at distances of approximately 50m away from the main fault. Samples B-16 and B-7 are located at distances of ~15m to ~20m to the fault respectively. Sample B-16 is from the most eastern rim of the sinter terrace. Two samples are potentially partially reset (B-5 and B-12). Both are within a distance of about 10m from the Malpais fault. These samples have a younger AHe age than the crystallization age but their error is still in the range of the U-Pb age. All other samples are younger than the crystallization age, showing a thermal overprint on their AHe age (B-2, B-3, B-8, B-9, B-10, B-11, B-13). These samples are within a distance of only a few meters to up to ~40m from the hydrothermally active normal fault. There are no fully reset samples, where AHe ages are equal to zero. Single grains that significantly are out of line with the others are excluded from the average age (marked grey in Table 5), but they are still included in the comparison between the modeled ages and the measured ages. These outliners can be the result of tiny inclusions or zoning in the actinide content of the dated apatite crystal. Sample 17 consistently shows higher AHe ages than its U-Pb age. As discussed in the previous section, sample 17 also plots into the latite field of the Streckeisen diagram as opposed to the other samples and its zircons contain more U and Th. Thus, sample 17 is most likely from a different lithology than the other samples, but it does not explain the anomalously old AHe age. This is most likely due to small fluid or mineral inclusions.

The ejection correction is an important part of the helium thermochronology. In the first approach the corrected ages were calculated by the assumption that the concentration of He α-emitting elements are homogeneous within the crystals. The laser ablation line measurement has shown variable patterns, both core and rim-zoned crystals occurred (Appendix pages vii to x). As a dominant character we can assume a weak dominance of the rim zonation, by about 15% in the outer most 10 µm. Thus we performed a control using the HeFTy software (Ketcham 2005) to calculate the magnitude of the influence of such zoning. Considering the typical properties of the Beowawe apatites (radius: 70 µm, U: 6 ppm, Th: 17 ppm, Sm: 370 ppm) the difference between the homogeneous assumption and the "average" rim zoned grains is approximately 100 to 200ka, thus actually negligible. Therefore, we performed all modelling procedures assuming homogeneous U-Th-Sm distributions and calculating the F_T correction value in the simplest way.

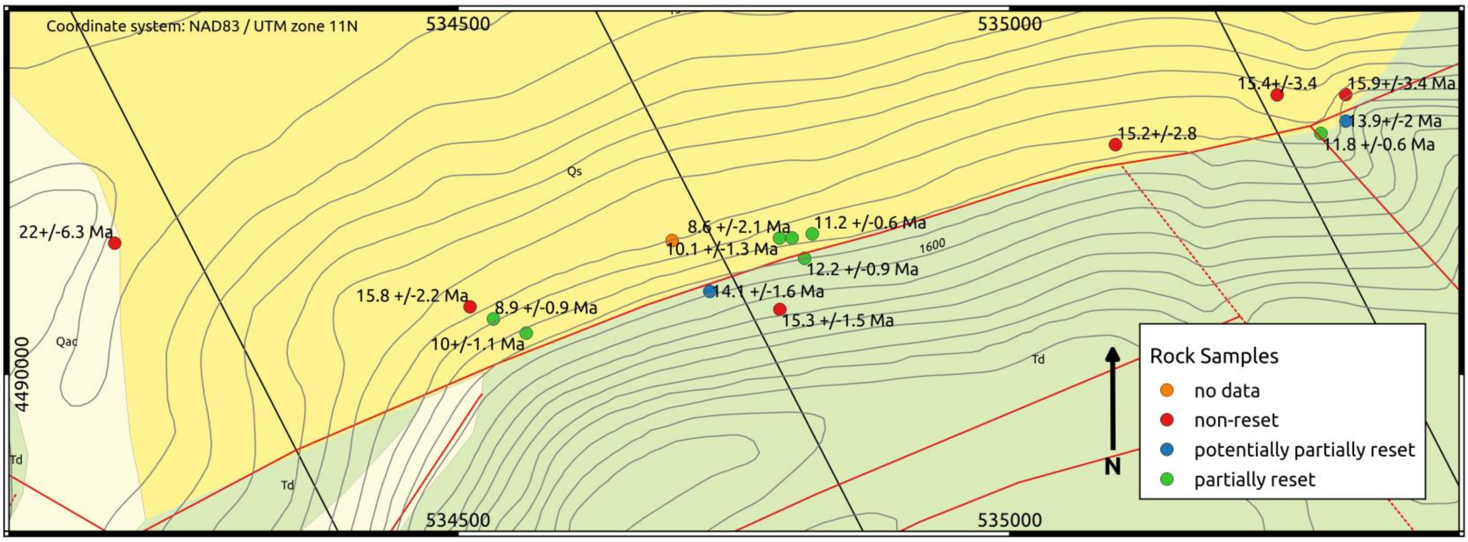

Figure 8 *Map showing the average AHe-ages of the sampled host rock. Samples marked with a green color are partially rese due to thermal conduction from the hydrothermally Malpais fault. They are clustered along this main fault. Samples marked with a blue color show a partially reset AHe age, but their error is within the range of the crystallization age, thus they are potentially reset. Samples colored in red have the same age as the rocks crystallization age. They were not thermally affected. Sample 17 shows a significantly higher age than its crystallization age. This sample has most likely inclusions that tamper the AHe ages.*

Table 5 Results of (U-Th)/He analysis

		He		U238			Th232				Sm			Ejection	*Uncorr.*	Ft-Corr.			Sample unweighted aver. ± 1 s.e.	
Sample	Sphere radius [µm]	vol. [ncc]	1s [%]	mass [ng]	1s [%]	conc. [ppm]	mass [ng]	1s [%]	conc. [ppm]	Th/U ratio	mass [ng]	1s [%]	conc. [ppm]	correct. (Ft)	*He-age [Ma]*	He-age [Ma]	2s [Ma]	2s [%]	[Ma]	[Ma]
B-1 a1	39.5	**0.018**	4.5	**0.006**	14.0	3.5	**0.022**	3.0	13.7	3.92	**0.550**	8.4	336	**0.59**	*9.6*	**16.3**	3.1	19.0		
B-1 a2	40.9	**0.023**	4.1	**0.005**	17.8	1.5	**0.015**	3.2	4.3	2.92	**0.511**	8.4	147	**0.59**	*14.7*	**24.8**	5.2	20.9		
B-1 a3	52.7	**0.030**	3.4	**0.009**	9.3	4.0	**0.027**	2.9	12.3	3.12	**0.731**	8.3	328	**0.69**	*11.7*	**16.8**	2.4	14.4		
B-1 a4	56.7	**0.032**	3.4	**0.010**	8.2	3.0	**0.030**	2.8	9.0	2.98	**0.945**	8.3	283	**0.72**	*10.6*	**14.7**	2.0	13.8	**15.8**	2.2
B-1 a5	68.6	**0.127**	1.8	**0.031**	3.0	5.3	**0.096**	2.5	16.4	3.08	**2.200**	8.2	377	**0.77**	*14.6*	**19.1**	1.8	9.4		
B-2 a1	94.9	**0.024**	3.8	**0.017**	5.1	4.3	**0.070**	2.5	17.5	4.10	**1.303**	8.2	328	**0.83**	*4.4*	**5.4**	0.6	10.9		
B-2 a2	106.5	**0.044**	2.8	**0.016**	5.4	2.9	**0.046**	2.7	8.6	2.94	**1.637**	8.2	302	**0.85**	*9.0*	**10.7**	1.1	10.0		
B-2 a3	104.1	**0.087**	2.0	**0.028**	3.3	7.7	**0.226**	2.4	63.1	8.16	**1.498**	8.2	418	**0.84**	*7.7*	**9.2**	0.7	7.4		
B-2 a4	81.7	**0.025**	3.5	**0.010**	8.1	4.7	**0.032**	2.8	14.7	3.14	**0.812**	8.3	371	**0.81**	*8.4*	**10.3**	1.2	12.0	**8.9**	0.9
B-3 a1	59.7	**0.108**	2.0	**0.046**	3.5	6.8	**0.209**	2.5	30.9	4.57	**2.675**	2.2	396	**0.729**	*7.61*	**10.44**	1.01	9.7		
B-3 a2	90.0	**0.033**	3.2	**0.017**	8.9	2.9	**0.054**	2.7	9.4	3.22	**1.362**	2.2	239	**0.834**	*6.77*	**8.11**	0.89	11.0		
B-3 a3	71.6	**0.042**	3.1	**0.019**	7.9	3.6	**0.054**	2.7	10.2	2.83	**1.188**	2.2	224	**0.795**	*8.36*	**10.52**	1.19	11.3		
B-3 a4	78.0	**0.031**	3.5	**0.013**	11.4	2.7	**0.039**	2.9	8.1	2.98	**0.952**	2.2	201	**0.792**	*8.61*	**10.87**	1.46	13.4	**10.0**	1.1
B-5 a1	72.7	**0.114**	1.9	**0.043**	2.3	6.5	**0.126**	2.5	19.0	2.91	**2.553**	2.8	384	**0.78**	*10.0*	**12.8**	1.0	8.0		
B-5 a2	67.5	**0.047**	2.7	**0.013**	5.5	6.3	**0.063**	2.6	30.2	4.78	**0.815**	3.8	392	**0.76**	*11.3*	**14.8**	1.5	10.1		
B-5 a3	90.5	**0.011**	5.3	**0.004**	24.7	2.2	**0.013**	3.5	7.5	3.50	**0.439**	4.8	256	**0.82**	*8.7*	**10.6**	2.2	21.1		
B-5 a4	67.9	**0.071**	2.2	**0.017**	4.5	4.9	**0.056**	2.6	15.7	3.19	**1.372**	3.1	387	**0.78**	*14.1*	**18.0**	1.6	9.0	**14.1**	1.6
B-6 a1	46.7	**0.024**	3.5	**0.009**	17.3	2.3	**0.026**	3.0	6.8	2.98	**0.510**	2.2	131	**0.658**	*10.36*	**15.75**	3.12	19.8		
B-6 a2	46.8	**0.036**	3.4	**0.012**	13.1	2.8	**0.036**	2.9	8.9	3.11	**0.629**	2.2	155	**0.664**	*11.73*	**17.67**	2.98	16.9		
B-6 a3	47.0	**0.009**	5.9	**0.004**	36.4	1.2	**0.013**	3.0	3.7	3.02	**0.321**	2.2	93	**0.681**	*7.63*	**11.20**	3.76	33.6		
B-6 a4	52.4	**0.027**	3.6	**0.008**	21.1	2.2	**0.024**	3.1	6.3	2.88	**0.537**	2.2	143	**0.709**	*12.45*	**17.57**	3.80	21.6	**15.5**	3.4
B-7 a1	55.9	**0.042**	2.7	**0.014**	9.9	2.9	**0.045**	2.8	9.3	3.16	**0.979**	2.2	204	**0.712**	*10.68*	**15.00**	1.99	13.2		
B-7 a2	51.6	**0.018**	4.3	**0.005**	30.9	1.5	**0.016**	3.1	4.8	3.23	**0.406**	2.2	118	**0.710**	*12.13*	**17.09**	4.70	27.5		
B-7 a3	61.3	**0.038**	3.1	**0.013**	11.0	2.7	**0.043**	2.8	8.6	3.24	**1.047**	2.2	210	**0.738**	*9.95*	**13.47**	1.81	13.4	**15.2**	2.8
B-7 a4	38.3	**0.020**	4.1	**0.005**	27.9	1.4	**0.015**	3.2	4.2	2.94	**0.469**	2.2	127	**0.575**	*12.77*	**22.20**	5.96	26.8		
B-8 a1	74.0	**0.052**	2.7	**0.026**	3.2	7.9	**0.071**	2.5	21.7	2.75	**1.465**	3.4	449	**0.78**	*7.9*	**10.1**	0.9	9.2		
B-8 a2	57.2	**0.033**	3.3	**0.013**	5.7	7.4	**0.038**	2.7	21.9	2.94	**0.822**	4.2	471	**0.72**	*9.4*	**13.1**	1.6	12.1		
B-8 a3	73.7	**0.017**	4.3	**0.011**	7.2	4.7	**0.034**	2.7	14.0	2.98	**0.924**	3.9	383	**0.78**	*5.3*	**6.9**	0.9	12.6		
B-8 a4	59.1	**0.058**	2.5	**0.027**	2.9	5.8	**0.086**	2.5	18.1	3.14	**1.819**	3.1	382	**0.73**	*7.7*	**10.5**	1.0	10.0	**10.1**	1.3
B-9 a1	72.6	**0.009**	5.9	**0.011**	7.4	8.6	**0.031**	2.8	24.9	2.89	**0.575**	5.4	461	**0.78**	*3.3*	**4.2**	0.6	15.4		
B-9 a2	74.8	**0.023**	3.9	**0.018**	4.4	5.8	**0.052**	2.6	17.0	2.94	**1.165**	3.5	384	**0.79**	*4.8*	**6.0**	0.7	11.0		
B-9 a3	63.5	**0.050**	2.8	**0.023**	3.3	4.8	**0.069**	2.5	14.7	3.03	**1.495**	3.7	319	**0.75**	*8.0*	**10.7**	1.1	10.2		
B-9 a4	45.7	**0.030**	3.2	**0.013**	5.3	5.8	**0.034**	2.7	14.6	2.53	**0.869**	3.7	373	**0.65**	*8.7*	**13.4**	1.8	13.4	**8.6**	2.1
B-10 a1	61.9	**0.041**	2.9	**0.017**	4.5	4.9	**0.053**	2.6	15.2	3.08	**1.355**	3.5	391	**0.73**	*8.2*	**11.2**	1.2	10.9		
B-10 a2	92.2	**0.024**	3.9	**0.010**	7.7	4.6	**0.032**	2.8	14.8	3.20	**0.756**	3.9	350	**0.83**	*8.4*	**10.1**	1.2	11.5		
B-10 a3	89.8	**0.122**	1.8	**0.040**	2.4	4.1	**0.204**	2.4	20.7	5.06	**3.298**	2.4	334	**0.82**	*8.7*	**10.6**	0.8	7.1		
B-10 a4	57.2	**0.045**	2.7	**0.016**	4.5	5.6	**0.060**	2.6	20.8	3.75	**1.261**	3.0	435	**0.71**	*9.1*	**12.7**	1.4	10.9	**11.2**	0.6
B-11 a1	76.2	**0.036**	2.8	**0.013**	5.5	4.2	**0.036**	2.7	11.7	2.78	**0.922**	3.8	298	**0.79**	*10.1*	**12.8**	1.3	10.0		
B-11 a2	83.6	**0.038**	3.0	**0.016**	4.8	7.8	**0.038**	2.7	18.5	2.37	**0.744**	3.7	364	**0.81**	*10.3*	**12.7**	1.3	9.8		
B-11 a3	75.3	**0.018**	4.1	**0.010**	7.4	8.4	**0.023**	2.9	20.8	2.46	**0.417**	4.3	370	**0.79**	*8.2*	**10.5**	1.4	12.9		
B-11 a4	106.5	**0.046**	2.7	**0.019**	4.0	7.1	**0.051**	2.6	18.5	2.61	**0.987**	3.6	361	**0.85**	*9.7*	**11.4**	0.9	8.2	**11.8**	0.6

Sensitivity analysis and model results

A sensitivity analysis was performed in order to quantify the impact of each tested parameter on the width of the partial and full reset zone on one side of the Malpais Fault over time. The x-axis shows the duration of hydrothermal activity (Figures 9 and 10). It also represents the location of the Malpais fault, where the y-axis is equal to zero and no apatites in the host rocks are thermally affected. Over long time scales, the host rock adjacent to the normal fault is heated due to conduction. This causes a rejuvenation of AHe ages in these rocks. The width of the area in which AHe ages are younger than their crystallization age is here referred to as the “width of partial reset zone”. The width of the area in which AHe ages are equal to zero is here referred to as the “width of full reset zone”. The width of the partial and full reset zone is pre-eminently a function of hydrothermal activity. Thus, we plotted the width of partial and full reset zone against the model runtime (Figure 9 and 10). The sensitivity of other variables such as fluid flux, fault damage zone width, background thermal gradient and exhumation rate were tested by changing one parameter at a time while keeping all other parameters at their base values. Base values are set to be 400 m²/sec for the fluid flux, 10m for the fault damage zone width, 0.04 °C m^{-1} for the background thermal gradient and 1e-4 m yr^{-1} for the exhumation rate. They are further marked by the red line in Figures 9 and 10. An exception had to be made for a flux of 500 and 600 m²/sec, where the fault damage zone width was increased to 20m due to numerical stability of the model run. As seen in the graphs of Figures 9 and 10, the partial and full reset zone increases with increasing hydrothermal activity. In general, the relationship between the runtime and the partial reset zone is relatively linear. The least sensitive parameter is the width of the fault damage zone. The differences in partial reset zone width are constantly about 5m per 10m of difference in fault damage zone width. Fluid flux has a great influence on the width of the partial reset zone perpendicular to the hydrothermally active fault for low flow rates. As fluid flux increases and reaches boiling temperatures at the surface, the differences become smaller. At high flow rates, this parameter becomes less sensitive. Same counts for background thermal gradient. Exhumation is highly sensitive. Notice the scale of the y-axis in comparison to the y-axis of the parameters fluid flux, damage zone width and background thermal gradient. For low exhumation rates, the impact on the partial reset width is relatively small. But with higher exhumation rates, the impact becomes very strong. As mentioned before, we did not find any fully reset sample. But a sensitivity study was still performed for the width of full reset zone. The parameters behave similar to those of the partial reset zone regarding their sensitivities. It just takes a much longer time for apatites to be fully reset than for them being partially reset. They also differ in their slope. At first the full reset zone grows faster as hydrothermal activity continues. Over larger time scales the slope flattens and the full reset zone becomes wider at a slower rate.

In Figure 11, different exhumation rates are plotted against the width of partial reset zone on one side of the hydrothermally active normal fault for different runtimes. The highest exhumation rate that we were able to test was 5e-4m yr^{-1}. A faster exhumation rate caused a numerical instability while modeling. The figure shows, that a relatively small increase in exhumation rates causes a large increase in the width of the partial reset zone to either side of a hydrothermally active area. The longer the hydrothermal system is active, the larger is the effect of exhumation on (U-Th)/He ages at a given thermal gradient. Thus, if there is hydrothermal activity on geological time scales, the area where AHe ages are rejuvenated becomes very large when exhumation or erosion take place at rates exceeding 1e-4m yr^{-1}.

We used temperature-depth profiles from two deep wells (85-15 and Batz1) provided by Chevron Resource Company (1979) as a target value for model calibration. Temperature overturns as seen in Figure 6 are due to lateral flow of hydrothermal fluids into a shallow aquifer. Estimates of lateral flow into thermal aquifers indicate a magnitude of about two thirds of the total up-flow of deep hydrothermal water (Olmsted & Rush 1987). Thus, the fluid flux inside the main fault was modeled according to Olmsted & Rush's water budget. About 1/3 of the total flux is discharged along the fault scarp. 2/3 of the modeled flux is discharged into subsurface conduits or aquifers. The location of aquifer flux was simulated by fitting the temperature-depth curve of the available deep well data. For the model setup, Batz1 is crossed by the profile A-A'. Beowawe 85-18 was interpolated onto the profile C-C'. Unfortunately no usable temperature-depth data was available for profile B-B'. The yellow line in both Figure 12 and 13 shows the best fit for the given temperature depth curve of the respective deep well. In both cases, a lower aquifer flux causes a negative inflection towards lower temperatures and an upper aquifer flux causes a positive inflection towards higher temperatures as compared to the background thermal gradient. The temperature-depth profile of well 85-18 was simulated with weaker aquifer fluxes in cross section C-C' (80 m^2/sec towards the fault in the lower aquifer and $330m^2/sec$ from the fault towards the valley in the upper aquifer) in comparison to the aquifer fluxes in cross section A-A' (400 m^2/sec towards the fault in the lower aquifer and $500m^2/sec$ from the fault towards the valley in the upper aquifer). Note that the deep well 85-18 is located at the western end of the hydrothermally active normal fault, while the deep well Batz1 is located right on top of the sinter terrace. The best fit (yellow line in Figures 12 and 13) suggests a hydrothermal activity of about 3200 years for profile A-A' and of about 1700 years for profile C-C'. For each model run, error statistics were calculated (Figure 17). The Mean Average Error (MEA) of the modeled temperature-depth curves versus the measured temperature-depth curves of the deep wells show a minimum at around 1700 years for well Batz1 and around 3200 years for well 85-18. Thus, the minimum statistical error (Figure 17) coincides with the visual best fit of the temperature depth curves in Figures 12 and 13. This is in geological time scales a very short duration and cannot make up for the sinter deposits, which according to Rimstidt & Cole (1983) needed around 200,000 years of hydrothermal activity to deposit.

For modeling the duration of thermal activity using AHe ages, we kept the aquifer fluxes as calibrated with the temperature-depth profiles. All other parameters were also kept as chosen for the respective profile in the previous model runs. For profile B-B'

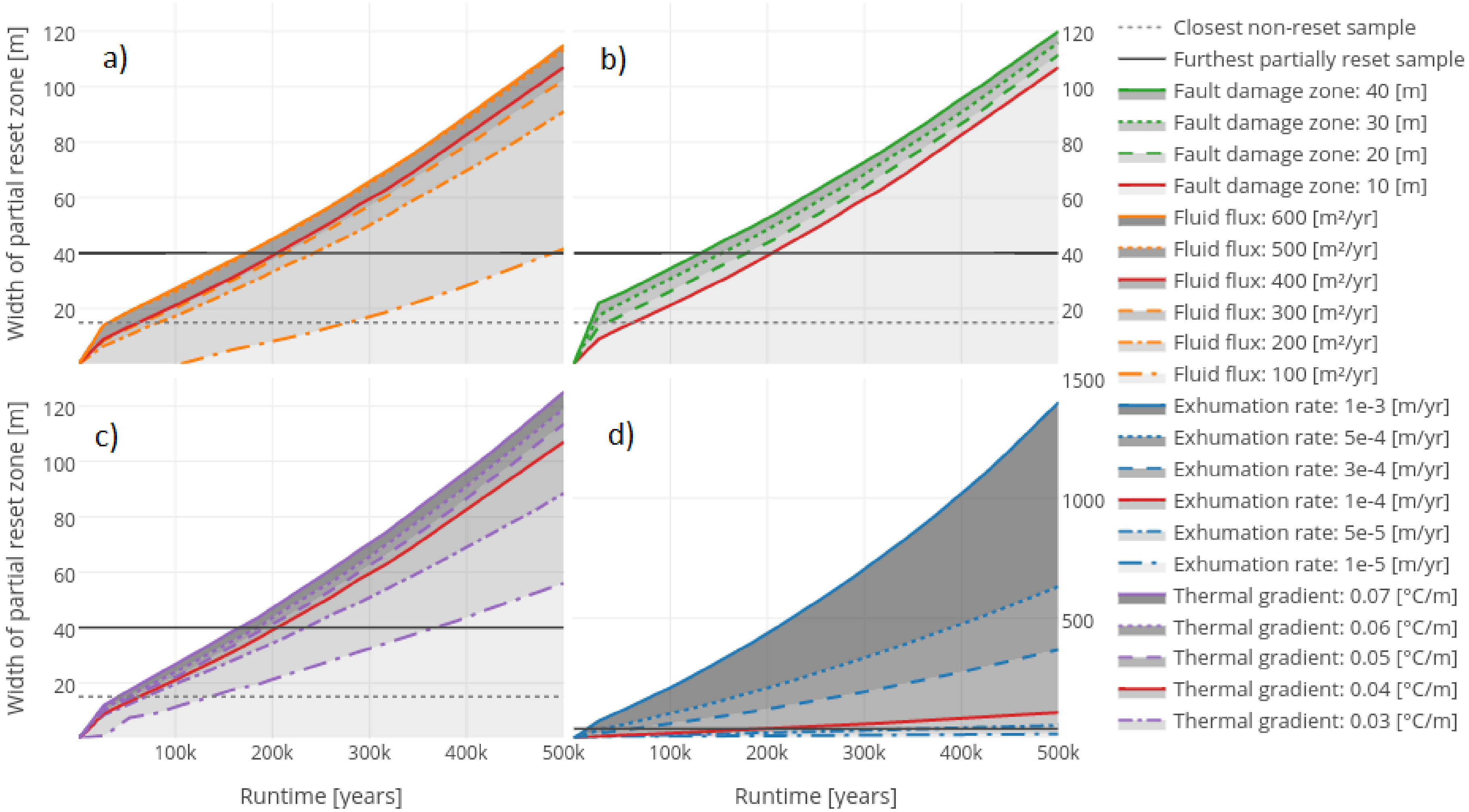

Figure 9 *Sensitivity of the size of the zone adjacent to one side of the hydrothermally active normal fault where AHe ages are partially reset. The analysis was performed for five parameters: hydrothermal activity (x-axis), a)fluid flux, b) fault damage zone width, c) background thermal gradient and d) exhumation rate. For each line in the graph, one parameter was changed while all other parameters were set to their base values, except for fluxes of 500 and 600 m²/sec, where the fault damage zone was increased to 20m due to numerical stability of the model run. Base values (red lines) are 400 m²/sec for the fluid flux, 10m for the fault damage zone, 0.04 °C/m for the thermal gradient and 1e-4 m/yr for the exhumation rate. Lateral flow in shallow layers connected to the fault was not taken into account. The most sensitive parameter is exhumation rate. An increase in exhumation rates leads to an exponential growth of the partial reset zone. The sensitivity for fluid flux, thermal gradient and fault damage zone are in a similar order of magnitude. Fluid flux and thermal gradient are more sensitive for small values and less sensitive for larger values. Fault damage zone is the least sensitive parameter.*

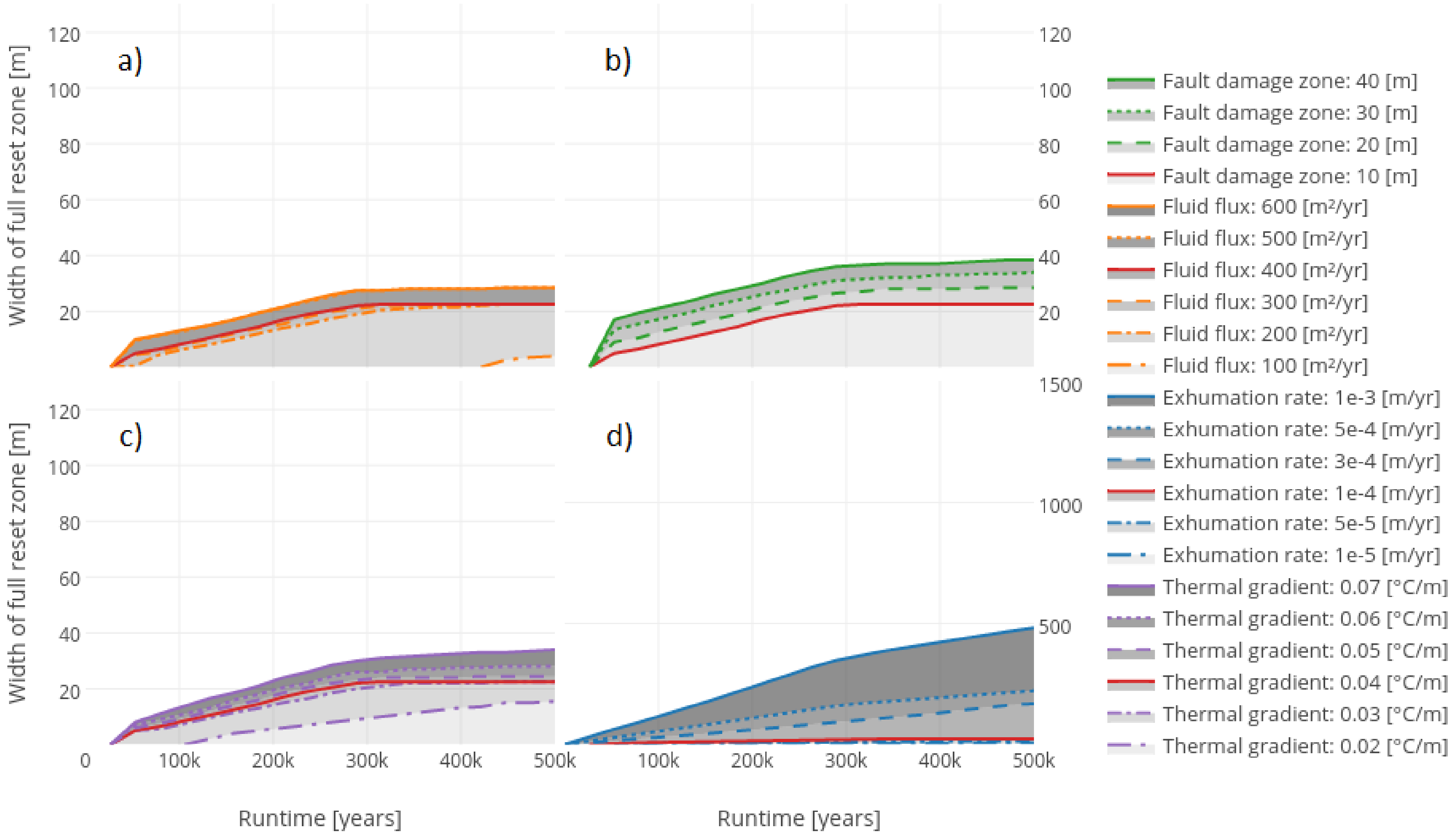

Figure 10 *Sensitivity of the size of the zone adjacent to one side of the hydrothermally active normal fault where AHe ages are fully reset. The analysis was performed for five parameters: hydrothermal activity (x-axis), a)fluid flux, b) fault damage zone width, c) background thermal gradient and d) exhumation rate. For each line in the graph, one parameter was changed while all other parameters were set to their base values, except for fluxes of 500 and 600 m²/sec, where the fault damage zone was increased to 20m due to numerical stability of the model run. Base values (red lines) are 400 m²/sec for the fluid flux, 10m for the fault damage zone, 0.04 °C/m for the thermal gradient and 1e-4 m/yr for the exhumation rate. Lateral flow in shallow layers connected to the fault was not taken into account. The parameters behave similar to those of the partial reset zone regarding their sensitivities. It just takes a much longer time for apatites to be fully reset than for them being partially reset. They also differ in their slope. At first the full reset zone grows faster as hydrothermal activity continues. Over larger time scales the slope flattens and the full reset zone becomes wider at a slower rate.*

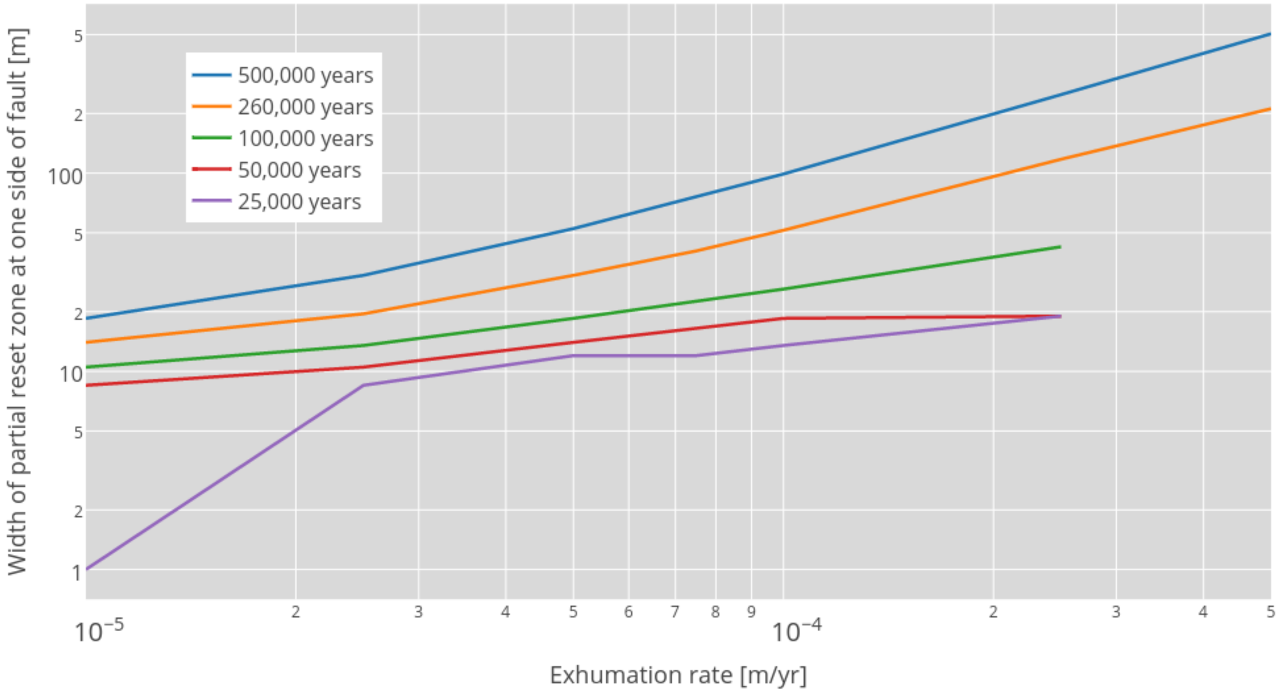

Figure 11: *Exhumation rate is plotted against the width of partial reset zone. Each colored line represents a different duration of hydrothermal activity. Axes are in logarithmic scale.*

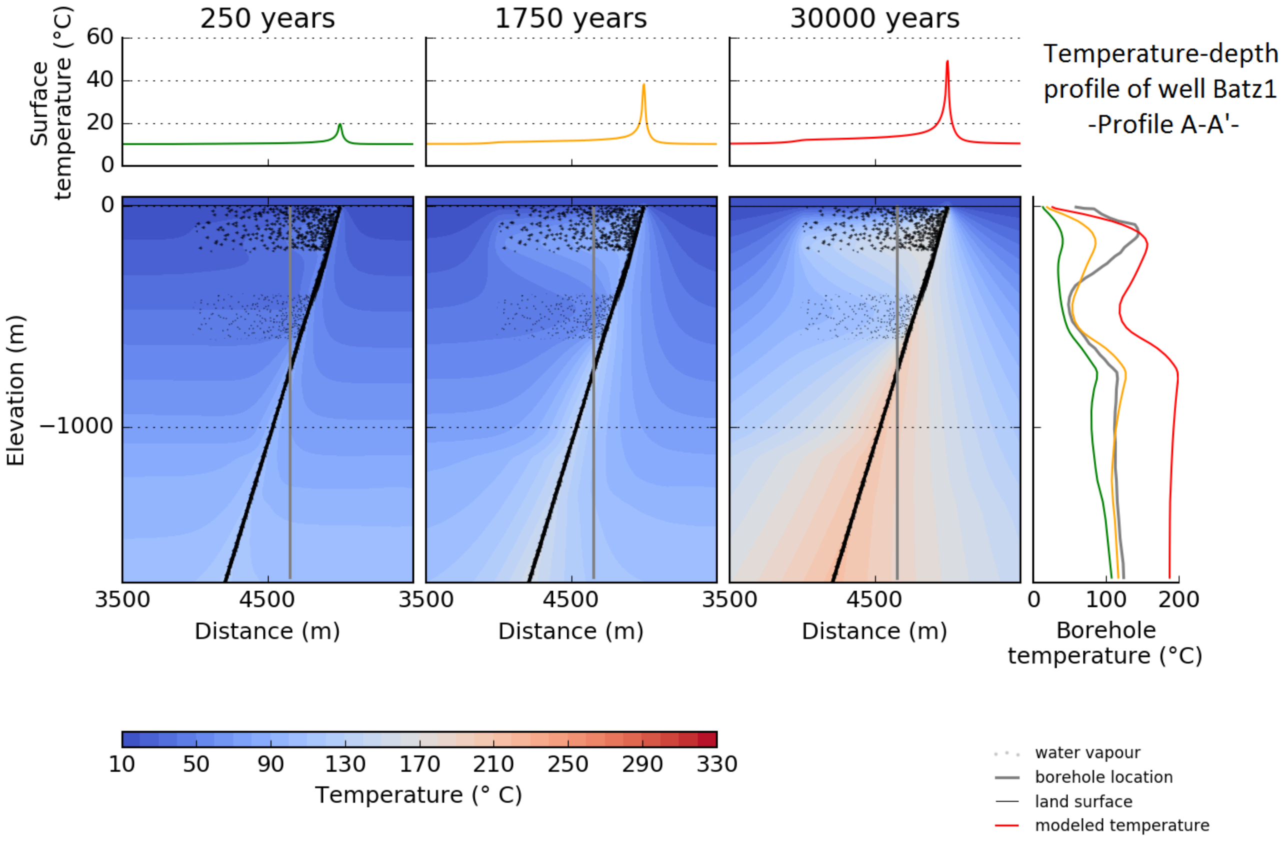

Figure 12 *Modeled hydrothermal activity using deep well Batz1 as target value. The grey vertical line in the three lower left panels shows the location and depth of Batz1; the arrows in the subsurface represent lateral flow in shallow layers connected to the Malpais fault (black line). The lower right panel shows the measured temperature-depth profile (grey line) and the modeled temperature-depth profile (green, yellow and red line) after the respective duration of hydrothermal activity shown above the upper panel. The best fit was achieved at 1750 years (yellow line) of activity.*

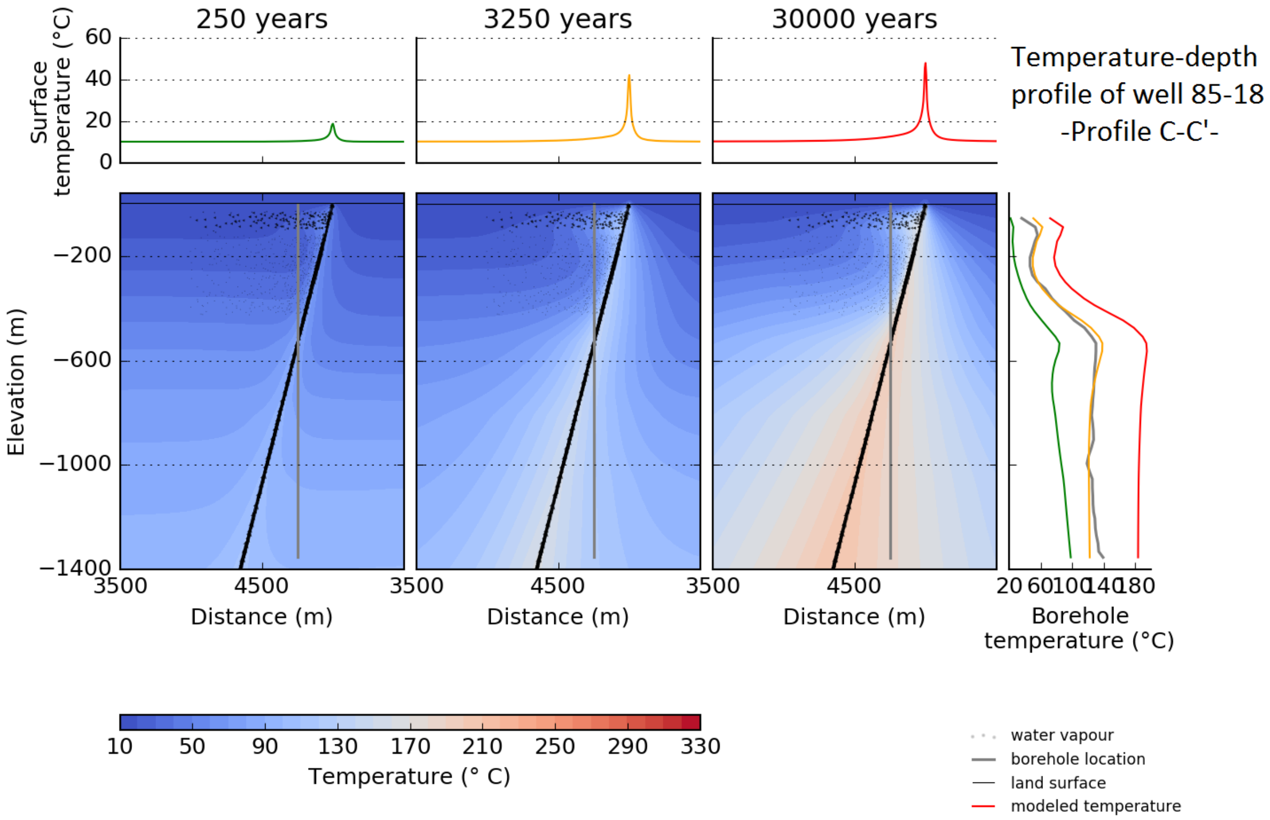

Figure 14 *Modeled hydrothermal activity using deep well Beowawe 85-18 as target value. The grey vertical line in the three lower left panels shows the location and depth of Beowawe 85-18; the arrows in the subsurface represent lateral flow in shallow layers connected to the Malpais fault (black line). The lower right panel shows the measured temperature-depth profile (grey line) and the modeled temperature-depth profile (green, yellow and red line) after the respective duration of hydrothermal activity shown above the upper panel. The best fit was achieved at 3250 years (yellow line) of activity.*

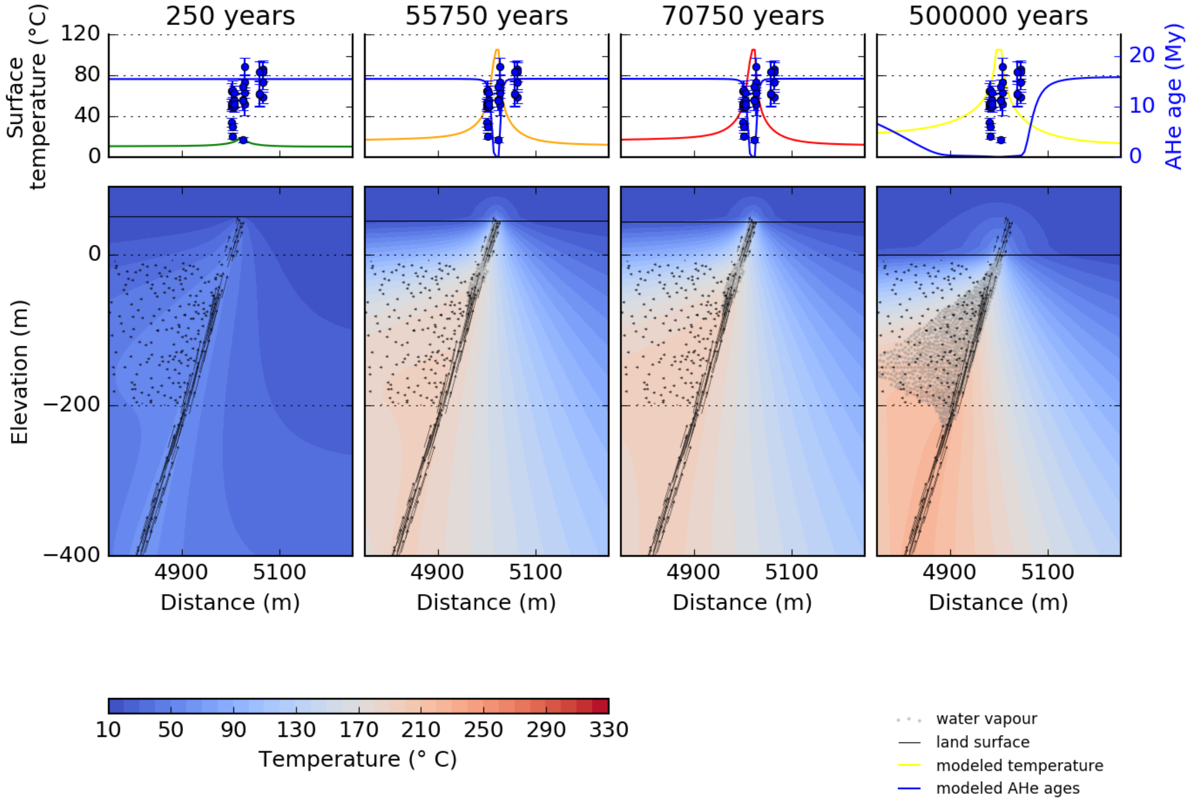

Figure 13 *Modeled hydrothermal activity for profile A-A' (see figure 1) using AHe ages as target value. The blue circles with error bars in the upper panel are measured AHe ages, the blue line represents modeled AHe ages over distance; opposing to temperature over distance (green, orange, red and yellow lines) after a certain duration of hydrothermal activity. Modeled and measured AHe ages achieved good fits within a time range between ~55k and ~70k of activity.*

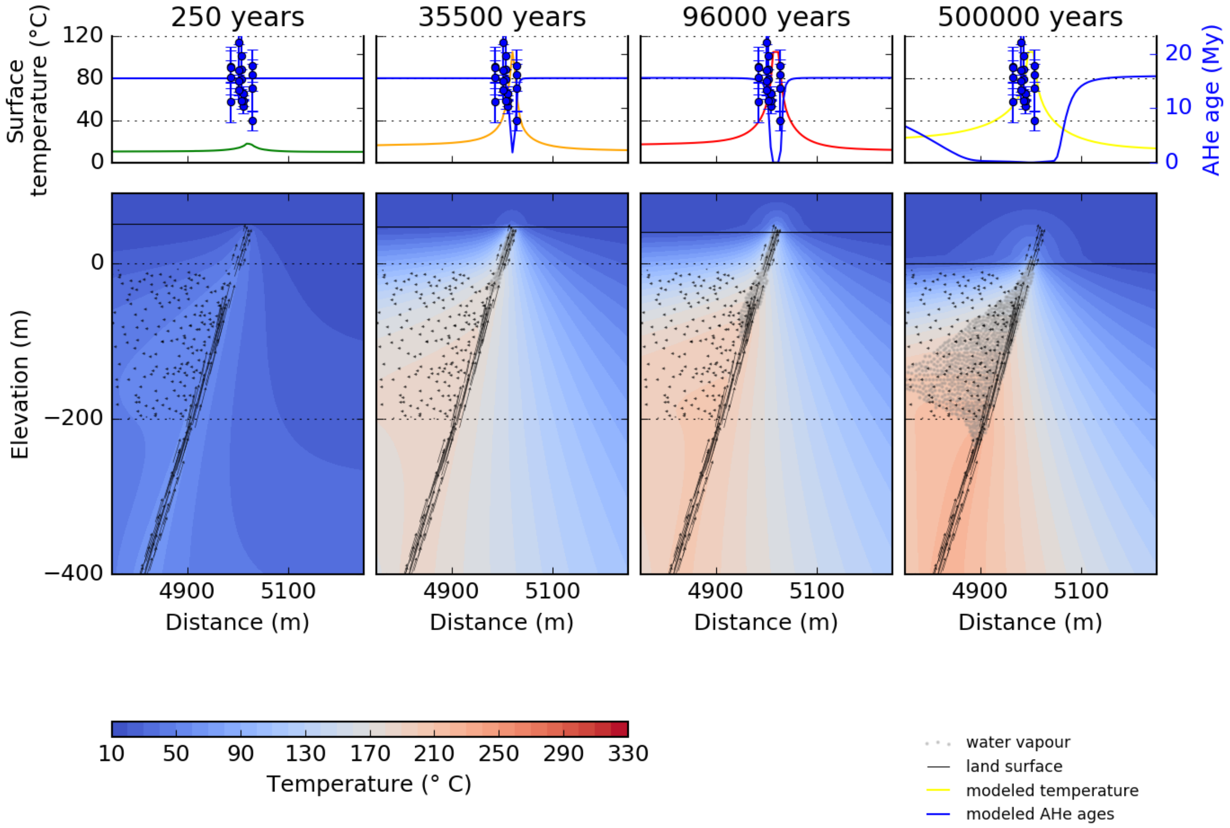

Figure 16 *Modeled hydrothermal activity for profile B-B’ (see figure 1) using AHe ages as target value. The blue circles with error bars in the upper panel are measured AHe ages, the blue line represents modeled AHe ages over distance; opposing to temperature over distance (green, orange, red and yellow lines) after a certain duration of hydrothermal activity. Modeled and measured AHe ages achieved good fits within a time range between ~35k and ~95k of activity.*

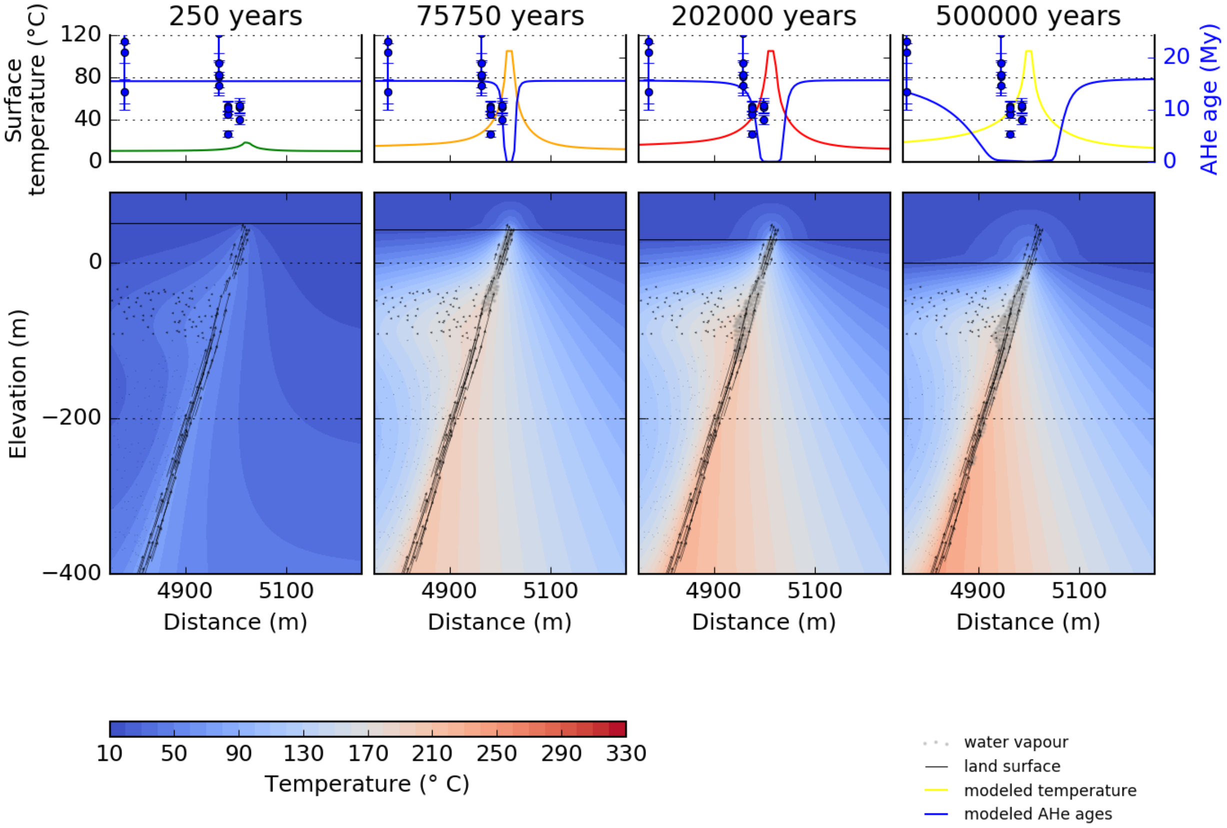

Figure 15 *Modeled hydrothermal activity for profile C-C’ (see figure 1) using AHe ages as target value. The blue circles with error bars in the upper panel are measured AHe ages, the blue line represents modeled AHe ages over distance; opposing to temperature over distance (green, orange, red and yellow lines) after a certain duration of hydrothermal activity. Modeled and measured AHe ages achieved good fits within a time range between ~75k and ~200k of activity.*

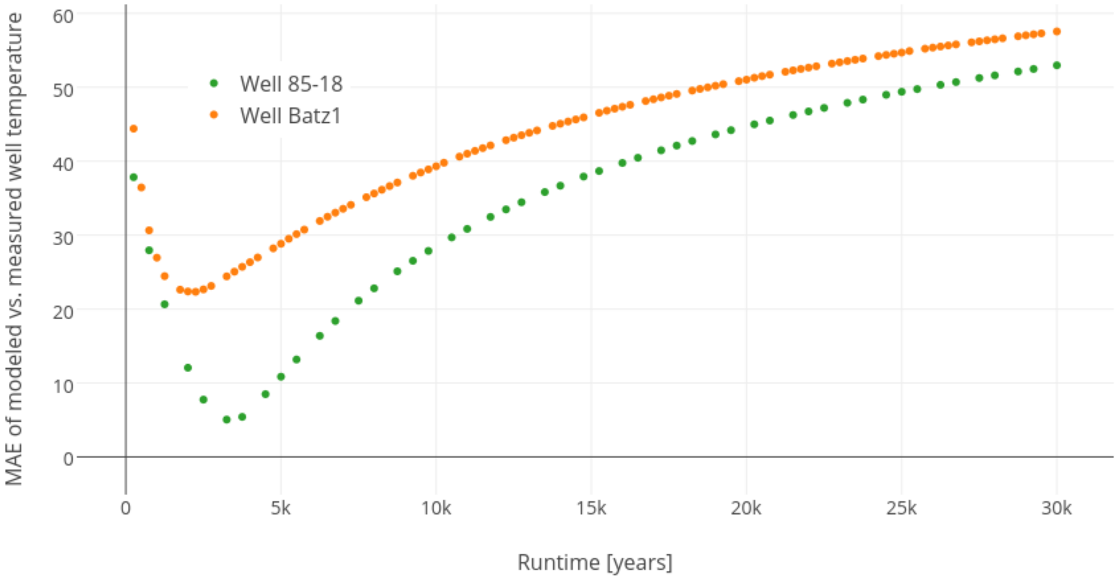

Figure 17 *Mean absolute error between modeled and measured well temperature over time. The Minimum values represent the best fit between measured borehole temperature in wells Beowawe 85-18 (green circles) and Batz1 (orange circles) at around 1700 and 3200 years respectively.*

similar conditions as for profile A-A’ were assumed and its parameters were transferred for modeling profile B-B’. Note that we used a fault damage zone width of 20m instead of the 10m used in the sensitivity analysis for quantifying hydrothermal activity. A wider fault damage zone assures a better numerical stability, but as the sensitivity analysis showed, it does not have a great effect on the width of partially reset zone. The duration of hydrothermal activity can be determined by comparing the AHe ages of the actual surface samples (blue dots in figure 14, 15 and 16) with the modeled AHe ages over time at that particular cross section. When the measured data is overlapping with the modeled data, the hydrothermal activity is quantified. In our study we were able to determine a time frame of how long the Beowawe system was active. Profile A-A’ reveals duration of hydrothermal fluid flow between 35,000 and 95,000 years. In profile B-B’ there was continuous activity for 55,000 to 70,000 years. And hydrothermal activity in profile C-C’ lasted between 75,000 and 200,000 years. There is not only a difference in quantified hydrothermal activity between modeled duration using temperature depth profiles versus AHe ages but results also vary between different locations. Hydrothermal activity determined by modeling with AHe ages is consistently longer than activity duration determined by temperature depth profiles, pointing towards a transient flow regime in the Beowawe hydrothermal system. Differences between the single profiles additionally suggest a shift in the location of hydrothermal activity over time.

Limitation

A limiting factor in modeling hydrothermal activity using surface samples is the actual location of the fault. It was very difficult to determine a clear fault scarp at the Malpais fault. Fumeroles and former geysers had a surface manifestation on top of the sinter terraces ~ 70m north of the fault mapped by Struhsacker (1980) and Layman (1984). Older sinter deposits of powdery consistency were located to the south of the mapped fault scarp on what seemed to be the foot wall. Obviously the locations of hydrothermal activity shifted along the Malpais normal fault over long time scales. The distances of the samples are within the ranges of tens of meters from the fault (i.e.
sample B-11, B-12 and B-13 are located at distances <10m and samples B-3, B-8, B-9 and B-10 are located at distance <20m of the hydrothermally active normal fault). Some of them are within the fault damage zone. A shift of the fault location would also shift the modeled AHe curve towards or away from the measured AHe ages of the samples, leading to a different fit between the modeled and the measured AHe ages and with that to different durations of hydrothermal activity.

AHe ages show different ages for the single crystals in a sample. This is due to a difference in size and possibly to inclusions or crystal damages. Thus, the model can either be fit to an average of the ages of a single sample or it can be fit to a certain range between the oldest and the youngest sample. We decided to show all ages and fit the model to the ones plot are close together. The modeled hydrothermal activity in Figures 14, 15 and 16 always show two fits (the inner two panels). Due to the ranging ages within a sample, both modeled AHe ages fitted the data. The quantified duration of activity therefore ranges between these two minimum and maximum activity values.

The large increase in temperature at shallow depth in Batz1 cannot be explained by lateral flow into an aquifer alone, because the aquifer flux would exceed the overall fluid flux. There have to be secondary faults that transport hot fluids to shallow depth underneath the sinter terrace in order to simulate this large temperature overturn in the temperature-depth profile. Besides that, the temperature-depth profile might be erroneous. It is rather difficult to explain, why the positive inflection of the temperature-depth curve in the Batz1 well at shallow subsurface depth exceeds the temperature where the well crosses the Malpais fault. Since the Malpais fault is the main conduit which transports the hot hydrothermal fluids from a deep reservoir to the surface. Also, the pressure at shallower depth is much less than at deeper depth so that it is rather unrealistic that the water reaches temperatures of over 140°C at a depth of ~100m below the surface but at depths between 700m to 1600m only ~100 to 120°C.

Using temperature-depth profiles for calibrating lateral subsurface fluid flow is a limiting factor for AHe modeling as well. Results show, that the modern system is only 2000-3000 years old. The hydrothermal system seems to be dynamic, however, so that the subsurface aquifer fluxes most likely changed over time as well.

CONCLUSIONS AND SUMMARY

We found that the AHe ages of the samples collected in the vicinity of a hydrothermally active fault were partially reset (Figure 8). With increasing distance from the normal fault, AHe ages were less significantly partially reset. Samples at a distance of ~50m were thermally unaffected, showing the same AHe ages than the crystallization (U-Pb) ages. The rocks adjacent to the active geysers and hot springs of the Beowawe hydrothermal system were heated over long periods of time. The thermal conduction into the host rock caused an area around the hydrothermally active Malpais fault where AHe ages in surface rocks were rejuvenated. Thermal conduction in rocks is a function of time and temperature flux. Using the new thermal model code beo.py (Luijendujk, unpublished) that simulates advective and conductive heat transfer, we were able to quantify the duration of hydrothermal activity.

First, the thermal model code was used to compare modeled temperature-depth profiles with measured temperature depth profiles. Temperature data of two deep wells in the vicinity of the hydrothermally active Malpais fault were used to simulate the fluid flow of the current system (Figures 12 and 13). These two profiles both showed inflections in their temperature curve that are caused by lateral, subsurface fluid flow. We found that the modern system was active for 1700 to 3200 years. One of the wells, Beowawe 85-18, is located at the western most end of the Beowawe sinter terrace (see map in Figures 1). A fit between the modeled temperature depth curve and the measured one was achieved at about 3200 years. The other deep well, Batz1, is located at the eastern part on top of the Beowawe sinter terrace. Here, model simulations resulted in a duration of hydrothermal activity of 1700 years.

After comparing the thermal model with borehole temperatures and modeling aquifer fluxes according to the temperature overturns in the temperature-depth profile of two deep wells, we used AHe data in surface samples to further quantify hydrothermal activity. AHe ages of 16 surface samples from around the Beowawe geysers and fumaroles were interpolated onto three profiles cutting the hydrothermally active Malpais fault orthogonally (see map in Figure 1). Luijendijk’s (unpublished) model code is also able to simulate the rejuvenation of AHe ages in surface samples along a cross section over geological time scales (Figures 14, 15 and 16). The modeled AHe ages were compared to the measured AHe ages in each of the three cross sections. Whenever there was a fit between the modeled and the measured AHe ages, it was possible to quantify the hydrothermal activity at that respective profile. Profile A-A’ crosses the Beowawe sinter terrace in the east. A fit between the modeled and the measured AHe ages was achieved between 35,000 and 96,000 years. Hydrothermal activity in profile B-B’ that crosses the middle of the sinter terrace lasted between 55,000 and 70,000 years. The duration of fluid flow in the western profile C-C’ ranged between 75,000 and 200,000 years.

Although there are variations between the modeled duration of hydrothermal activity between the different profiles, the time spans come close to each other at around 70,000 years in all three profiles. However, the modeled activity using AHe ages as target values contradicts with the modeled activity using borehole temperature as target values. The AHe model predicts a much longer duration than the thermal model using borehole temperature data. Due to this fact, we conclude that hydrothermal activity is transient. Both methods can only model ongoing hydrothermal activity. A difference in the results using two kinds of target values suggests that hydrothermal fluid flow occurs periodically. Additionally, a variance in modeled hydrothermal activity between different locations along the hydrothermally active normal fault in Beowawe is an indicator for shifting locations of activity along that fault.

Without lateral flow, overturns in temperature depth profiles are only visible for a relatively short period of time, since the overturn dissipates over time due to conduction. Because the large sinter deposits along the Malpais fault are evidence for hydrothermal activity lasting at least 200,000 years (Rimstidt & Cole 1983), the thermal overturns in some of the temperature-depth profile might be evidence for transient, episodic flow with periods of higher and lower hydrothermal activity over geological time scales (Howald et al. 2015). Leatherman (2010) modeled geochemical reaction paths of fluid inclusions and found that fluid pathways must have shifted over time. Our results show a contradiction in the modeled hydrothermal activity using downhole temperatures versus AHe ages. The time of continuous activity that was determined by modeling AHe ages over time with the thermal model code showed significantly longer durations than the time of activity calculated using temperature depth profiles. This points to a transient system that shifts its locations of hydrothermal activity along the Malpais fault or that has less active periods, supporting Howald et al.'s (2015) and Leatherman's (2010) results. It is difficult though, to quantify these transient flows. Howald et al. (2015) suspect that earthquakes have an influence on the permeability of hydrothermal fluid pathways and therefore affect fluid flux over time. They were able to show a correlation between recorded earth quakes and a change in stable isotopes composition of the hydrothermal fluids, enabling for a quantification of temporal fluctuations in hydrothermal activity. Nolan & Anderson (1934) even report seasonal fluctuations in hydrothermal fluid flow, indicated by more energetic activity during the winter months. Supporting evidence for a transient system is the fact that our samples did not contain a single fully reset apatite. The AHe model predicts a zone of up to 20m to both sides of the hydrothermally active normal fault where all apatites are fully reset, showing a (U-Th)/He age of zero, if the system was active for about 200,000 years. Since there are only partially reset AHe samples at a distance of up to 40m to the fault, there had to be periods where the system was not active at that location, so that temperatures were either not high enough to cause rejuvenation in AHe ages or where the ^{4}He started accumulating anew after being reset.

Some parameters that are needed as model input are rather uncertain or may have changed over time. A sensitivity analysis was performed to test how much the most important parameters influence the width of the partial reset zone. This zone is the area where AHe ages are rejuvenated due to thermal conduction from the hydrothermally active fault and is used as a target value for the thermal AHe model. Fault damage zone width and discharge do not have such a large effect on the width of the partial reset zone. The background thermal gradient is slightly more sensitive than fluid flux and fault damage zone width, but the magnitude decreases with increasing values for background thermal gradient. The most sensitive parameter is the exhumation rate. Increasing values for exhumation or erosion cause a huge growth in the width of the partial (and also the full) reset zone around the center of hydrothermal activity.

The model shows that air temperature significantly affects heat conduction in surface samples. The alteration zone of thermochronometers is smaller at the surface than in the subsurface, where heat conduction is unaffected by the surface-air boundary. Exhumation rates determine to what extend a thermal effect is visible in (U-Th)/He data. Thus, exhumation has a strong impact on thermochronometers. Combining thermochronometers with high temperature geochronometers like Zircon U-Pb reveal low-temperature, upper crustal processes and their thermal history from emplacement to erosion (McInnes et al. 2005). The U-Pb content in our samples was not only determined to know the crystallization age of the samples, but also to use these U-Pb ages as the background age for AHe analysis. With that we were able to determine the maximum exhumation rate to be 1e-4m yr^{-1} in the Beowawe area. Figures 9, 10 and 11 show how exhumation rates influences the width of partial reset zone. According to Herman et al. (2013) erosion rates vary globally within orders of magnitude , ranging from 0.01mm yr^{-1} to 10m yr^{-1}. An exhumation rate of 5e-4 m yr^{-1} is resulting in a partial reset zone width of 200m to each side of the hydrothermally active area after 200,000 years of activity. With an exhumation rate of 1e-3m yr^{-1} this zone increases to a 500m wide zone in each direction.

All things considered, two main scientific findings resulted from this study. First, low temperature thermochronology in combination with numerical modeling can be used to quantify hydrothermal activity. The new model code beo.py (Luijendijk, unpublished) is a strong tool for modeling the thermal evolution of a hydrothermal system over geological time scales using both borehole data and (U-Th)/He data as target values. This method, however, is limited in quantifying transient flow. In future, this method should be tested for transient flow by modeling different combinations of periodic hydrothermal activity and by collecting more samples for a higher data resolution. Secondly, the sensitivity study reveals an extreme sensitivity of AHe ages to exhumation. This has to be kept in mind, when quantifying hydrothermal activity by using low-temperature thermochronometers. The effect of hydrothermal fluid flow on low temperature thermochronometers in combination with high exhumation or erosion rates might have an influence on the interpretation of thermochronological datasets in general and should be studied in more detail.

OUTLOOK

To enhance the resolution of our method, more samples have to be taken. Because a first model run predicted a thermal overprint mainly within a distance of tens of meters from the heat source, we sampled close to the Malpais fault. As reported by Zoback (1979), there is a much older manifestation of the Beowawe hydrothermal system at White Canyon, only 250m south of the Malpais fault at the foot of a fault striking parallel to the Mailpais fault. Evidence for early hydrothermal activity at White canyon is a chalcedony/carbonate vein. No sinter deposits are present at White canyon. According to Zoback (1979) and White (1970), this might be due to heat loss by conduction in an early sluggish geothermal system with a slow flow of fluids to the surface. Additionally, slight fluctuations in pH can change precipitation of silica and carbonate. In a future study, additional sampling around that fault would be prudent, as well. I'd expect the AHe ages to be older even adjacent to the surface manifestation of the older Beowawe system. This is due to the fact that this part was apparently active for a much shorter period of time and it was active before the system reached its modern manifestation at the Malpais rim. In addition, a slower upward flow of hydrothermal fluids would mean less heat conduction to the surface. It would be interesting to compare AHe data of the White Canyon outcrop to the data collected at the Malpais fault in this study.

Zoback lists a carbonate breccia deposit at the splay of the main range front fault (~8km to the East of the Beowawe geysers) that suggests early low temperature hydrothermal activity (below 100°C). Both the chalcedony vein and the carbonate breccia are supposed to be older than the basaltic andesite eruptions (Mid-Miocene, 16.7 Ma). Because AHe dating is sensitive to very low temperatures, an early low temperature hydrothermal system would be detectable with this method. In a future study, sampling close to this carbonate breccia is suggested to determine the thermal overprint. This, in addition to sampling around White Canyon, may mark the beginning of hydrothermal activity in the Beowawe area. This is important to further narrow down the timespan of hydrothermal activity.

Since our data indicates a transient fluid flow along the Malpais normal fault, it is important to be able to delineate the locations and durations of hydrothermal activity. To improve dating of hydrothermal activity in general, closely spaced sampling around the hydrothermal system is advisable. If the hydrothermal system is located along a normal fault, like it is the case of the Beowawe system, samples should also be taken at larger distances to the fault in order to better determine the exhumation rate. Heat conduction is expected to be different in the hanging wall compared to the foot wall. This is mainly due to continuing fault block movement and sediment fillings on top off the hanging wall. Like Gorynski et al. (2014) did, surface samples should be taken over a long distance (~5km) along a profile crossing the hydrothermal system in order to exactly determine local exhumation.

A sensitivity analysis on fault location with regards to measured AHe ages of the samples is suggested in order to determine the magnitude of difference in modeled hydrothermal activity. Statistical errors between modeled and measured AHe ages also have to be included in order to quantify hydrothermal activity more precisely. It would also be interesting to test the effect of exhumation on AHe ages in a hydrothermal system with regards to different thermal gradients to see how large the effect is on the width of partial and full reset zone to the sides of the hydrothermal system.

REFERENCES

Banerjee, A. et al., 2011. Deep permeable fault-controlled helium transport and limited mantle flux in two extensional geothermal systems in the Great Basin, United States. *Geology*, 39(3), pp.195–198.

Bateni, S.M. & Entekhabi, D., 2012. Relative efficiency of land surface energy balance components. *Water Resources Research*, 48(4), pp.1–8.

Benoit, D. & Stock, D., 1993. A Case History of Injection at theBeowawe, Nevada Geothermal Reservoir. *Geothermal Resources Council Transaction*, 17, pp.473–480.

Bense, V.F. et al., 2013. Fault zone hydrogeology. *Earth-Science Reviews*, 127, pp.171–192. Available at: http://dx.doi.org/10.1016/j.earscirev.2013.09.008.

Blackwell, D.D., 1983. Heat Flow in the Northern Basin and Range Province. *Geothermal Resources Council SPECIAL REPORT No.13*, pp.81–92.

Caine, J., Evans, J.P. & Forster, C.B., 1996. Fault zone architecture and permeability structure. *Geology*, 24(11), pp.1025–1028.

Childs, C. et al., 2009. A geometric model of fault zone and fault rock thickness variations. *Journal of Structural Geology*, 31(2), pp.117–127.

Cole, D.R. & Ravinsky, L.I., 1984. Hydrothermal alteration zoning in the Beowave geothermal system, Eureka and Lander Counties, Nevada. *Economic Geology*, 79(4), pp.759–767.

Dunkl, I. et al., 2008. Brief introduction to the Windows program Pepita: data visualization, and reduction, outlier rejection, calculation of trace element ratios and concentrations from LA-ICP-MS data. In P. Sylvester, ed. *Laser ablation ICP-MS in the Earth Sciences: Current practices and outstanding issues*. Vancouver, British Columbia: Mineralogical Association of Canada, pp. 334–340.

Eaton, G.P., 1982. The Basin and Range Province: Origin and Tectonic Significance. *Annual Review of Earth and Planetary Sciences*, 10, pp.409–440.

Epperson, I.J., 1982. Beowawe, Nevada, Well Testing: History and Results. *Geothermal Resources Council Transaction*, 6, pp.257–260.

Farley, K.A., Wolf, R.A. & Silver, L.T., 1996. The effects of long alpha-stopping distances on (U-Th)/He ages. *Geochimica et Cosmochimica Acta*, 60(21), pp.4223–4229.

Faulds, J.E., Garside, L.J. & Oppliger, G.L., 2003. Structural Analysis of the Desert Peak-Brady Geothermal Fields, Northwestern Nevada: Implications for Understanding Linkages between Northeast-Trending Structures and Geothermal Reservoirs in the Humboldt Structural Zone. *Geothermal Resources Council Transactions*, 27, pp.859–864.

Flowers, R.M. et al., 2009. Apatite (U-Th)/He thermochronometry using a radiation damage accumulation and annealing model. *Geochimica et Cosmochimica Acta*, 73(8), pp.2347–2365.

Frei, D. & Gerdes, A., 2009. Precise and accurate in situ U-Pb dating of zircon with high sample throughput by automated LA-SF-ICP-MS. *Chemical Geology*, 261(3–4), pp.261–270. Available at: http://dx.doi.org/10.1016/j.chemgeo.2008.07.025.

Garg, S.K. et al., 2007. Characterization of geothermal reservoirs with electrical surveys: Beowawe geothermal field. *Geothermics*, 36(6), pp.487–517.

Gorynski, K.E. et al., 2014. Apatite (U-Th)/He thermochronometry as an innovative geothermal exploration tool: A case study from the southern Wassuk Range, Nevada. *Journal of Volcanology and Geothermal Research*, 270, pp.99–114. Available at: http://dx.doi.org/10.1016/j.jvolgeores.2013.11.018.

Gross, L. et al., 2007. A Python Module for PDE-Based Numerical Modelling. In B. Kågström et al., eds. *Applied Parallel Computing. State of the Art in Scientific Computing SE - 33*. Lecture Notes in Computer Science. Springer Berlin Heidelberg, pp. 270–279.

Hager, C., 2009. A new MATLAB-based helium modeling package (HeMP) for thermal history recovery from single and multi thermochronometer (U-Th)/He data and data arrays. In *Geological Society of America Abstracts with Programs, Vol. 41, No. 7*. p. 487.

Herman, F. et al., 2013. Worldwide acceleration of mountain erosion under a cooling climate. *Nature*, 504(7480), pp.423–426. Available at: http://dx.doi.org/10.1038/nature12877.

Hickey, K.A. et al., 2014. The Brevity of Hydrothermal Fluid Flow Revealed by Thermal Halos around Giant Gold Deposits: Implications for Carlin-Type Gold Systems. *Economic Geology*, 109(5), pp.1461–1487. Available at: http://econgeol.geoscienceworld.org/content/109/5/1461.abstract.

Hickey, K.A., Dipple, G.M. & Barker, S.L.L., 2009. Duration of hydrothermal fluid flow responsible for Carlin-type Au-deposits, Nevada: implications for the scale of thermal haloes and the distal physiochemical expression of mineralization. *Thermal and geochemical footprints of low-temperature sedimentary rock-hosted hydrothermal Au-systems: Identifying far-field vectors toward ore Year 2 Technical Summary*, p.Section 5. Available at: https://www.eoas.ubc.ca/~khickey/TotalReport_April2009.pdf.

Hickey, K.A. & Tosdal, R.M., 2012. *Spatial - temporal patterns in hydrothermal flow in Carlin-type Au-deposits in north-central Nevada mapped using apatite fission-track thermochronology ; USGS MRREP # 06HQGR0182*,

Howald, T. et al., 2010. Duration, and Rate of Silica Deposition Along the Malpais Fault Zone, Beowawe Geyser Field, NV. In *Geological Society of Nevada Symposium*.

Howald, T. et al., 2015. Evidence for long timescale (>103 years) changes in hydrothermal activity induced by seismic events. *Geofluids*, 15(1–2), pp.252–268.

Iovenitti, J.L. & Epperson, Jr., I.J., 1981. *Beowawe Geothermal Area Evaluation Program - Final Report*, San Francisco, CA.

Jackson, S.E. et al., 2004. The application of laser ablation-inductively coupled plasma-mass spectrometry to in situ U-Pb zircon geochronology. *Chemical Geology*, 211(1–2), pp.47–69.

Jungers, M.C. & Heimsath, A.M., 2016. Post-tectonic landscape evolution of a coupled basin and range: Pinaleño Mountains and Safford Basin, southeastern Arizona. *Bulletin of the Geological Society of America*, 128(3–4), pp.469–486.

Ketcham, R. a., 2005. Forward and Inverse Modeling of Low-Temperature Thermochronometry Data. *Reviews in Mineralogy and Geochemistry*, 58(1), pp.275–314.

Lachenbruch, A.H., 1978. Heat flow in the Basin and Range province and thermal effects of tectonic extension. *Pure and Applied Geophysics PAGEOPH*, 117(1–2), pp.34–50. Available at: http://pubs.er.usgs.gov/publication/70012657.

Layman, E.B., 1984. A Simple Basin and Range Fault Model for the Beowawe Geothermal System, Nevada. *Geothermal Resources Council, Transactions*, 8, pp.451–455.

Leatherman, M., 2010. *Geochemistry and Reaction Path Modelling of the Beowawe Hydrothermal System, Nevada: A Barren End-Member Epithermal System*. University of Missouri-Columbia.

Ludwig, K.R., 2012. User's Manual for Isoplot 3.75, a geochronological toolkit for Microsoft Excel. *Berkeley Geochronology Center Special Publication*, (5), pp.1–72.

Luijendijk, E., 2012. The role of fluid flow in the thermal history of sedimentary basins: Inferences from thermochronology and numerical modeling in the Roer Valley Graben, southern

Netherlands. , p.198.

Meesters, A.G.C.A. & Dunai, T.J., 2002a. Solving the production–diffusion equation for finite diffusion domains of various shapes Part I. Implications for low-temperature (U–Th)/He thermochronology. *Chemical Geology*, 186(3–4), pp.333–344. Available at: http://www.sciencedirect.com/science/article/pii/S0009254101004223.

Meesters, A.G.C.A. & Dunai, T.J., 2002b. Solving the production–diffusion equation for finite diffusion domains of various shapes Part II. Application to cases with a-ejection and nonhomogeneous distribution of the source. *Chemical Geology*, 186(3–4), pp.57–73.

Middleton, W.M., 1961. *Report on Beowawe Nevada Geothermal Steam Wells for Magma-Vulcan Thermal Power Project*, Los Angeles, CA.

Nolan, T.B. & Anderson, G.H., 1934. The geyser area near Beowawe, Eureka County. *American Journal of Science*, 27, pp.215–229.

Nuriel, P., 2014. Faults (U-Series). In *Encyclopedia of Scientific Dating Methods*.

Olmsted, F.H. & Rush, F.E., 1987. Hydrogeologic reconnaissance of the beowawe geysers geothermal area, Nevada. *Geothermics*, 16(1), pp.27–46.

Olmsted, F.H., Welch, A.H. & Ingebritsen, S.E., 1986. Shallow subsurface temperature surveys in the basin and range province, U.S.A.-I. Review and evaluation. *Geothermics*, 15(3), pp.251–265.

Paces, J.B. & Miller, J.D., 1993. Precise U-Pb ages of Duluth Complex and related mafic intrusions, northeastern Minnesota: Geochronological insights to physical, petrogenetic, paleomagnetic, and tectonomagmatic processes associated with the 1.1 Ga Midcontinent Rift System. *Journal of Geophysical Research*, 98(B8), p.13997.

Parsons, T.E., 1995. The basin and range province: Chapter 7. In K. H. Olsen, ed. *Continental rifts: evolution, structure,and tectonics*. Elsevier, pp. 277–324. Available at: http://pubs.er.usgs.gov/publication/70133658.

Poulet, T. et al., 2012. Escript-RT: Reactive transport simulation in Python using escript. *Comput. Geosci.*, 45, pp.168–176.

Reiners, P.W., 2002. (U-Th)/He chronometry experiences a renaissance. *EOS Transactions American Geophysical Union*, 83(3), p.21,26-27. Available at: http://adsabs.harvard.edu/abs/2002EOSTr..83...21R.

Reiners, P.W. & Farley, K.A., 2001. Influence of crystal size on apatite (U-Th)/He thermochronology: An example from the Bighorn Mountains, Wyoming. *Earth and Planetary Science Letters*, 188(3–4), pp.413–420.

Rimstidt, J.D. & Cole, D.R., 1983. Geothermal Mineralization. I: the Mechanism of Formation of the Beowawe, Nevada, Siliceous Sinter Deposit. *American Journal of Science*, 283(8), pp.861–875.

Schaa, R., Gross, L. & du Plessis, J., 2016. PDE-based geophysical modelling using finite elements: examples from 3D resistivity and 2D magnetotellurics. *Journal of Geophysics and Engineering*, 13(2), p.S59. Available at: http://stacks.iop.org/1742-2140/13/i=2/a=S59.

Sláma, J. et al., 2008. Plesovice zircon - A new natural reference material for U-Pb and Hf isotopic microanalysis. *Chemical Geology*, 249(1–2), pp.1–35.

Smith, C., 1983. Thermal hydrology and heat flow of Beowawe geothermal area, Nevada. *Geophysics*, 48(5), pp.618–626. Available at: http://library.seg.org/doi/abs/10.1190/1.1441492.

Struhsacker, E.M., 1980. The Geology of the Beowawe Geothermal System, Eureka and Lander Counties, Nevada. *University of Utah Research Institute, Earth Science Laboratory*, pp.1–78.

Umeda, K. et al., 2007. Thermochronology of non-volcanic hydrothermal activity in the Kii Peninsula, Southwest Japan: Evidence from fission track dating and helium isotopes in paleo-hydrothermal fluids. *Radiation Measurements*, 42(10), pp.1647–1654.

White, D.E., 1998. The Beowawe Geysers , Nevada , Before Geothermal Development. *U.S. Geological Survey Bulletin*, pp.1–28.

Wiedenbeck, M. et al., 1995. Three Natural Zircon Standards for U-Th-Pb, Lu-Hf, Trace Element and Ree Analyses. *Geostandards Newsletter*, 19(1), pp.1–23.

Wisian, K.W., Blackwell, D.D. & Richards, M., 1999. Heat Flow in the Western United States and Extensional Geothermal Systems. *Twenty-Fourth Workshop on Geothermal Reservoir Engineering*, p.8.

Wolf, R.A., Farley, K.A. & Kass, D.M., 1998. Modeling of the temperature sensitivity of the apatite (U–Th)/He thermochronometer. *Chemical Geology*, 148(1–2), pp.105–114.

Young, R.A. ed., 1995. *The Rietveld Method*, Oxford University Press.

Zoback, M.L.C., 1979. A geologic and geophysical investigation of the Beowawe Geothermal Area, North-Central Nevada. *Geological Sciences*, 16.

APPENDIX

Sample locations and notes from fieldwork

Date	Sample	Latitude [°, WGS84]	Longitude[°, WGS84]	Distance to Fault [m]	Comments Sarah Louis	Comments Elco Luijendijk
10.15.2015	B1	-116.5923474	40.56060024	56 N	Bedrock underneath a sinter terrace. Close to well in the E.	Outcrop of 2 m thick 5m wide layered sinter overlying and cementing loose bedrock. at bottom 30 cm of bedrock. Sample from 15 cm size bedrock fragments at bottom. Volcanic sample, black-gray groundmass, withg up to 2 mm phenocrysts, quartz, feldspar, pyroxene/amphibole?GPS pt approx. 3 m north of outcrop
	B2	-116.5920974	40.56050024	38 N	Outcrop in upper part of the sinter terrace; above B1. 14.8 m E of B1	Photo from 1.5 m in front of outcrop. Loc: on slope 17 m above loc sample 1. White sinter approx 5 m to east and minor 2 m to west of outcrop. Sample: coarser grained than sample b1. Max crystal size 1.5 mm quartz feldspar pyroxene. Outcrop 2 m wide 1.5 m high. GPS pos 888.
	B3	-116.5917474	40.56038354	15 N	Outcrop just above sinter terrace; 30 m E of B1.	4 by 2 m outcrop. At slope approx 30 m above sinter terrace. Photo from 2.5 m north of outcrop.
	B4	-116.5901807	40.56113354	48 N	Close to road, across from well (Vulcan2/Beowaw 33..???). Bedrock is stuck in the sinter deposit.	Large outcrop of powdery sinter. 5 m high 50 m long. On road 10 m se of easternmost well.
	B5	-116.5897807	40.56071684	7 S	Bedrock above sinter deposit. Hard rock.	on slope, 30 m above b4
10.16.2015	B6	-116.5836974	40.56230024	35 N	Bebris-flow within the sinter on sinter terrace.	Samples from debris flow below 1.5 m thick sinter deposit. Approx 70 cm if debris flow exposed angular poorly sorted bedrock fragments floating in silt matrix. Photo 1.5 m in fort of outcrop.
	B7	-116.5854307	40.56190024	19 N	Outcrop above E part of terrace. Strike/dip: 190/43.	From southward dipping dacite. Lots of calcite coating strongly fractured. Partly overlain by debris flows at several m distance.
	B8	-116.5890307	40.56115024	20 N	Bedrock right next to upper sinter terrace in the E. Some rocks are strongly altered and hard. Cracks with sinter filling cross through the bed rock.	Fractured bedrock with sinter in fillings. High fracture density approx 1 per 1.5 m horizontally. Conjugate vertical set at 30 degree angle and horizontal along bedding plane.
	B9	-116.5888974	40.56115024	17 N	15 m E from B8. Thick cracks filled with sinter.	15 m along road east from sample b8z. Fractured dacite with many silica veins. up to 5 cm thick veins
	B10	-116.5886807	40.56118354	15 N	Another 15 m from B9 along the outcrop towards E.	32 m east along road of sample b8. Measured. Fractured bedrock again altered bedrock around veins as in last 2 samples.
	B11	-116.5832307	40.56198354	10 N	Right on E flank of canyon/fault. Red rock/hard.	Red colored ground mass dacite? Still large up to 1.5 mm crystals quartz amphibole or pyroxene. Outcrop in canyon that is eastern edge of sinter terrace.
	B12	-116.5829640	40.56208354	8 S	~24m E from B11. Rock is strongly fractured.	
10.17.2015	B13	-116.5887640	40.56098354	4 S	About 10-15 m above B8 and ~ 15-20 m above active fumerol. Bedrock very hard.	
	B14	-116.5890307	40.56056684	44 S	Another 15-20 m above B13. A few m SW of active fumerol --> uneffected rock.	
	B15	-116.5901419	40.56034377	37 S	On top. (Thunderstorm!)	Dacite strongly fractured. With cylindrical structures. Check sample no. At bottom of upper cliff straight above the eastern end of road on top of terrace and eastern most well on upper level
	B16	-116.5829640	40.56230024	14 N	On top. Next to B12.	Approx 5 m from wall and 4 m higher
	B17	-116.5961474	40.56113354	242 N	On the W most edge.	Sample from bedrock outcrop adjacent to gully. Exactly at boundary between sinter terrace and bedrock. Nice dacite with large amphibole or pyroxene crystals.

Pictures of sample locations from Elco Luijendijk and Sarah Louis

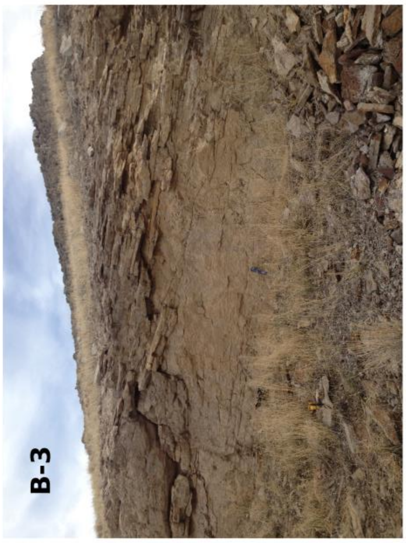

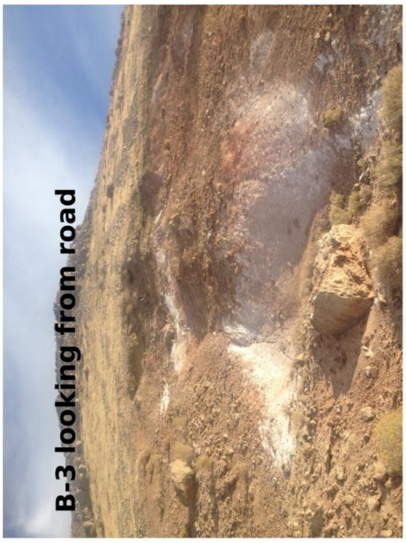


B-7 close up

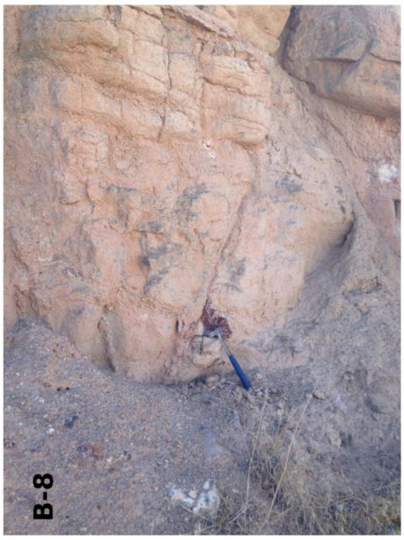
B-8

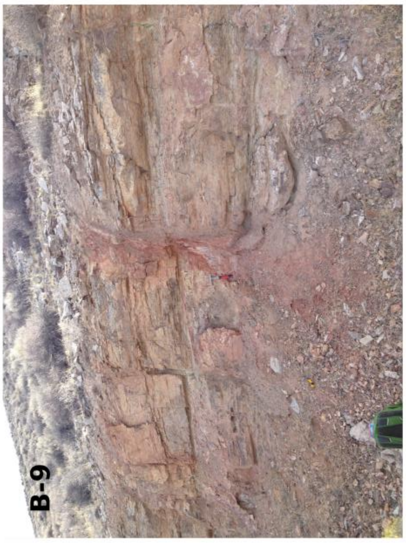
B-9


B-10

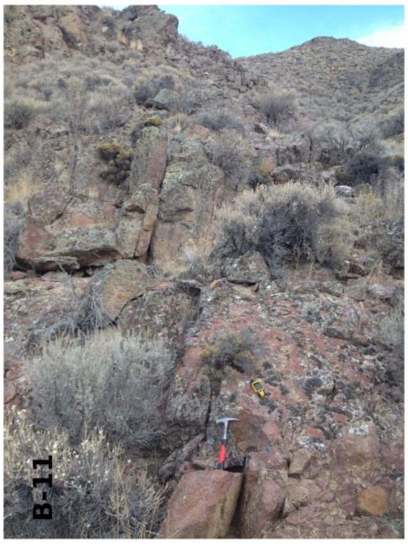
B-11

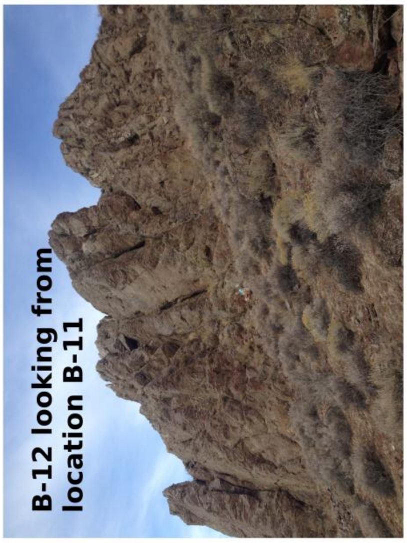
B-12 looking from location B-11


B-15


B-16 looking from locationB-15

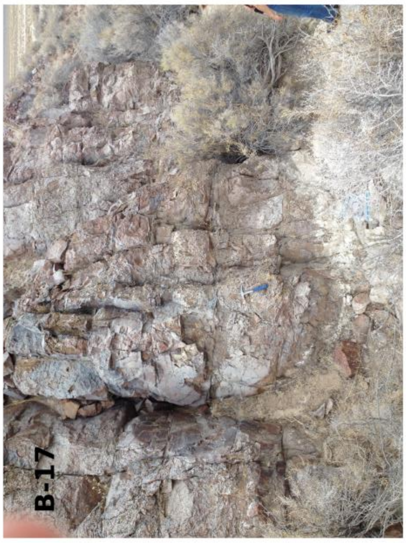
B-17

Sample fractions after sieving

Sample	petrograph	Total [g]	>1 mm [g]	500µm-1mm [g	250-500 µm [g	<250 µm [g	<250 µm [%	ST2 [g]	ST1 [g]	ST 1/2
B-1	dacite	1055.8	189	237.4	127.4	502	47.5	137.32	22.98	0.17
B-2	dacite	928.4	136.7	228.9	99.3	463.5	49.9	100.71	21.89	0.22
B-3	dacite	1166.39	133	297.8	135.99	599.6	51.4	159.28	23.67	0.15
B-4	dacite	1119.1	78.4	347.2	151.2	542.3	48.5	120.78	22.76	0.19
B-5	dacite	939.8	119.8	313.9	124.2	376.5	40.3	71.47	29.37	0.41
B-6	dacite	1276	77.4	33.4	202.8	661.8	51.9	183.86	13.759	0.07
B-7	dacite	1167.58	77.7	372.3	177.5	540.08	46.3	143.5	19	0.13
B-8	dacite	1413.1	142.9	462.9	183.7	608.5	43.5	95.67	20.23	0.21
B-9	dacite	1576.5	109.6	517.1	222.2	727.6	46.1	95.42	20.45	0.21
B-10	dacite	789.3	49.5	237.8	146.1	355.9	45.1	28.27	3.49	0.12
B-11	dacite	1399.7	62.8	421.9	235.9	679.1	48.5	214.5	23.06	0.11
B-12	dacite	1326.08	177.3	395.3	197.3	556.18	41.9	181.25	23.57	0.13
B-13	dacite	1172.8	96.2	373.5	149.9	553.2	47.2	94.08	16.71	0.18
B-14	dacite	1408.3	143.8	462.7	190.4	600.7	42.6	117.34	17.74	0.15
B-15	dacite	1840.7	129.1	517.8	261	932.8	50.7	267.3	18.68	0.07
B-16	dacite	1577.5	105.7	483.1	248.1	740.6	46.9	256.17	17.95	0.07
B-17	dacite	1477.2	113.4	415.3	196.1	752.4	50.9	186.6	24.97	0.13

XRD results measured on July 8th 2016 by Volker Karius and Sarah Louis

Device	Philips X'Pert MPD
Rietveld software	AutoQuan 2.8.0.1
Tube	Cu Kα
Voltage [kV]	40
Current [mA]	30
Soller slit [rad]	0.04
Divergence slit [°]	0.5
Mask [mm]	20
Anti Scatter slit [°]	0.5
Reciving slit [mm]	0.2
Scan mode	step scan
Step (°2Theta)	0.02
Time/step [s]	10
Internal Standard	20 wt% ZnO

SiO2 (Quarz) [%]	K-Fsp [%]	Plagioclase [%]
20	46	34
6	21	73
7	27	66
22	23	54
20	17	63
19	19	62

Batch 1		Mineral Phase [wt%]	±3σ	Mineral Phase [wt%]	±3σ	Mineral Phase [wt%]	±3σ
Probe	Qualitätsparameter (1-rho) [%]	amorph content		Cordierite		Cristobalite	
SL-B-4	0.76	5.20	4.20			6.26	1.23
SL-B-5	0.63	8.37	2.91	2.86	0.42	2.32	0.81
SL-B-8	0.66	4.20	3.30			2.74	0.63
SL-B-9	0.76	2.90	4.80			11.14	2.85
SL-B-14	0.68	5.20	3.30	0.75	0.33	9.74	2.04
SL-B-17	0.75	5.40	3.30	0.20	0.28	9.20	0.99

Batch 1	Mineral Phase [wt%]	±3σ	Mineral Phase [wt%]	±3σ	Mineral Phase [wt%]	±3σ	Mineral Phase [wt%]	±3σ
Probe	Tridymite		Diopside		Garronite		Goethite	
SL-B-4	9.85	0.84			1.55	1.11	1.75	0.81
SL-B-5	9.80	1.32					5.79	0.96
SL-B-8	9.56	1.44					3.19	0.84
SL-B-9	10.52	0.72			0.88	1.08	0.72	0.96
SL-B-14	4.19	1.26					4.62	1.17
SL-B-17	3.29	1.92	1.91	0.72			6.24	1.08

Batch 1	Mineral Phase [wt%]	±3σ	Mineral Phase [wt%]	±3σ	Mineral Phase [wt%]	±3σ	Mineral Phase [wt%]	±3σ
Probe	Hematite		Kaolinite		Microcline		Albit	
SL-B-4	2.28	0.45	6.75	1.11	14.16	3.81	2.68	2.31
SL-B-5	1.17	0.22			7.93	2.01	2.04	0.69
SL-B-8	1.51	0.25	1.68	0.75	11.43	2.76	4.89	1.41
SL-B-9	2.27	0.39			11.56	4.05	3.40	2.19
SL-B-14	1.65	0.21			8.02	1.89	9.17	1.77
SL-B-17	1.09	0.17			9.13	1.95	7.37	1.47

Batch 1	Mineral Phase [wt%]	±3σ	Mineral Phase [wt%]	±3σ	Mineral Phase [wt%]	±3σ	Mineral Phase [wt%]	±3σ
Probe	Andesine		Quartz		Sanidine		Smectite	
SL-B-4	7.70	1.74	6.02	0.45	23.37	2.73	12.40	3.30
SL-B-5	26.25	1.41	2.92	0.19	24.11	1.59	6.43	1.20
SL-B-8	23.04	1.47	3.17	0.27	24.38	1.56	10.14	1.68
SL-B-9	23.49	1.59	2.52	0.36	22.30	2.85	8.75	2.85
SL-B-14	21.38	1.56	4.28	0.21	25.81	1.80	5.18	1.05
SL-B-17	22.81	1.68	1.10	0.14	27.16	1.71	5.16	1.41

Laser ablation profiling perpendicular to the c-axis performed on December 17th 2016 by István Dunkl

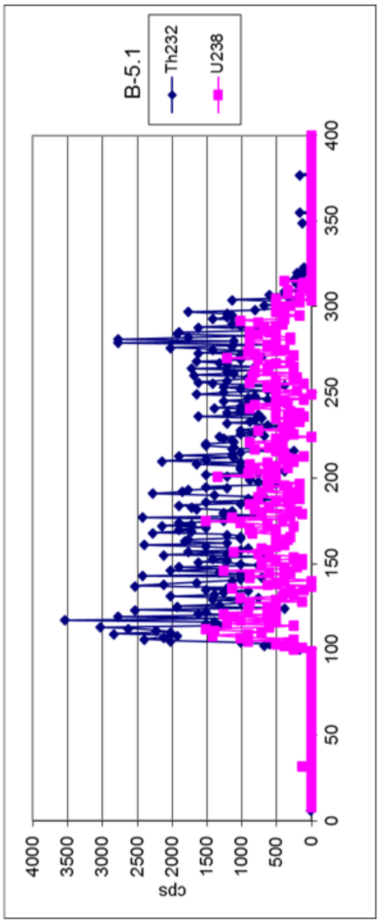

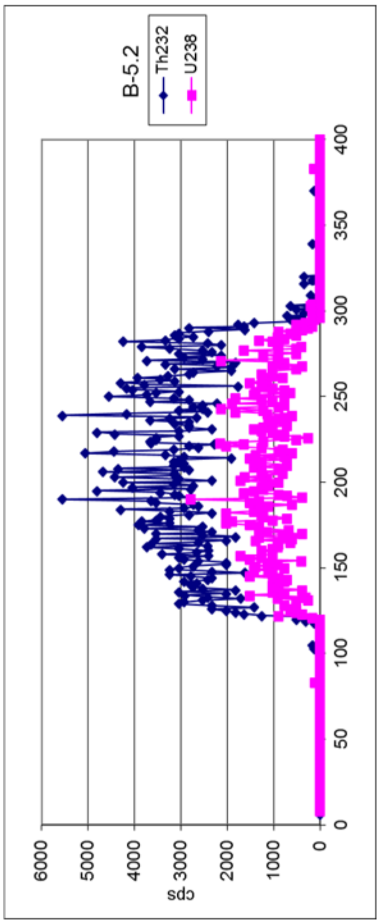

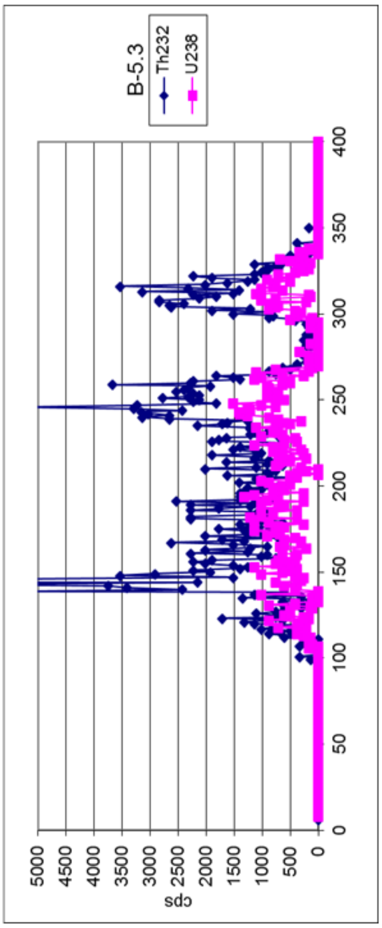

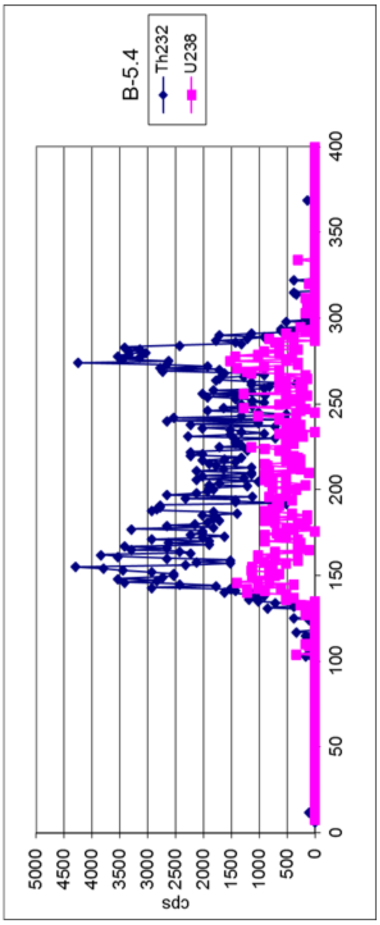

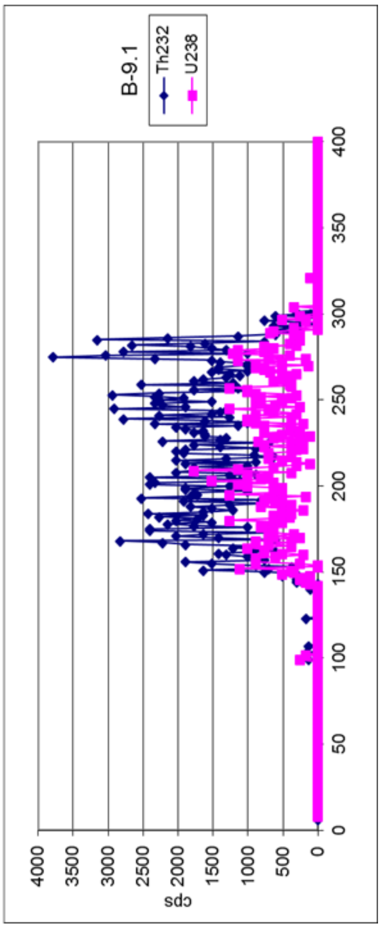

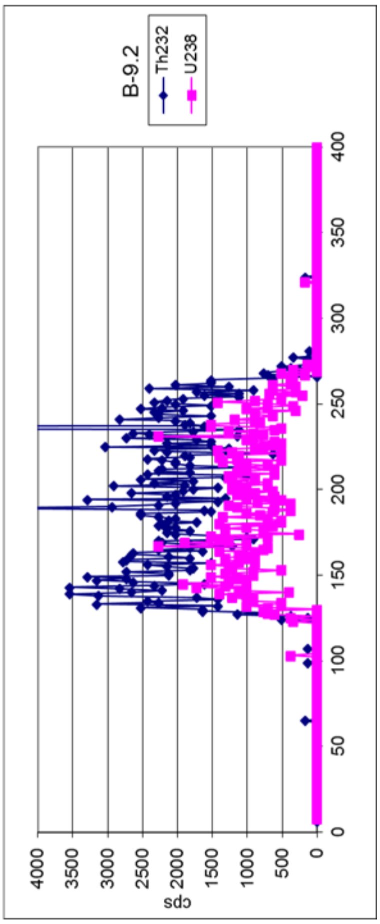

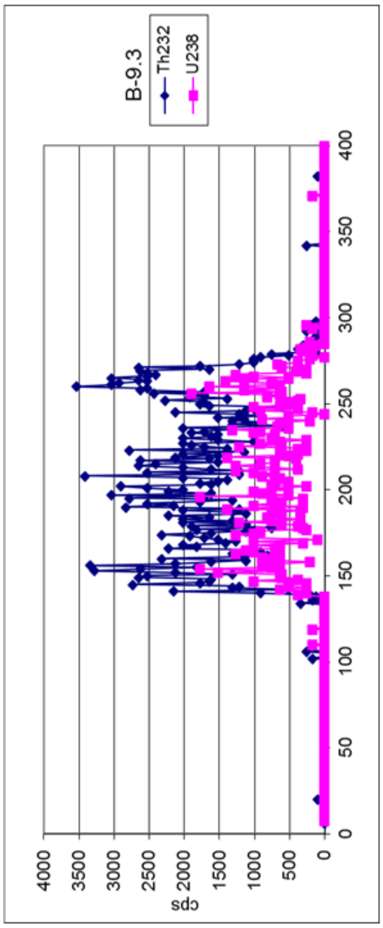
B-9.3
Th232
U238
cps
4000
3500
3000
2500
2000
1500
1000
500
0
0
50
100
150
200
250
300
350
400

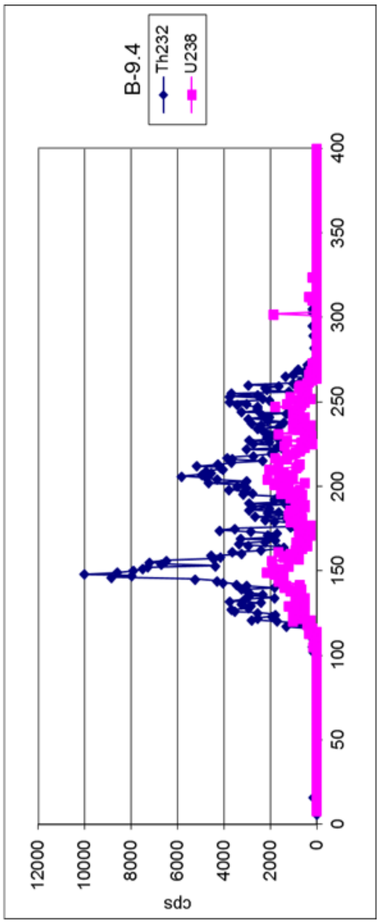
B-9.4
Th232
U238
cps
12000
10000
8000
6000
4000
2000
0
0
50
100
150
200
250
300
350
400

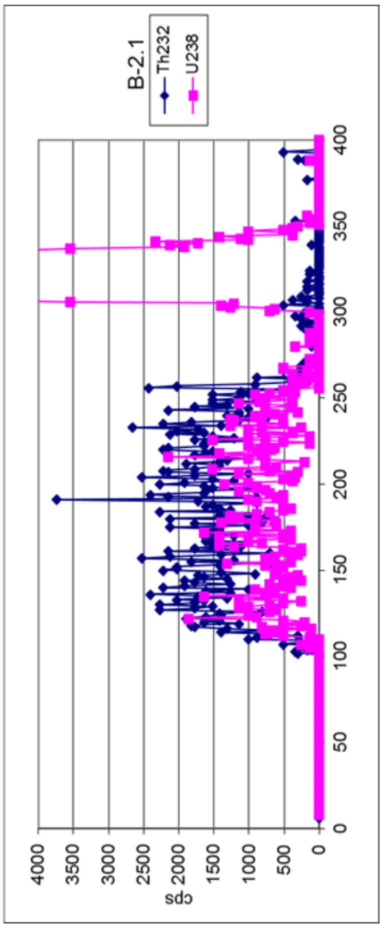
B-2.1
Th232
U238
cps
4000
3500
3000
2500
2000
1500
1000
500
0
0
50
100
150
200
250
300
350
400

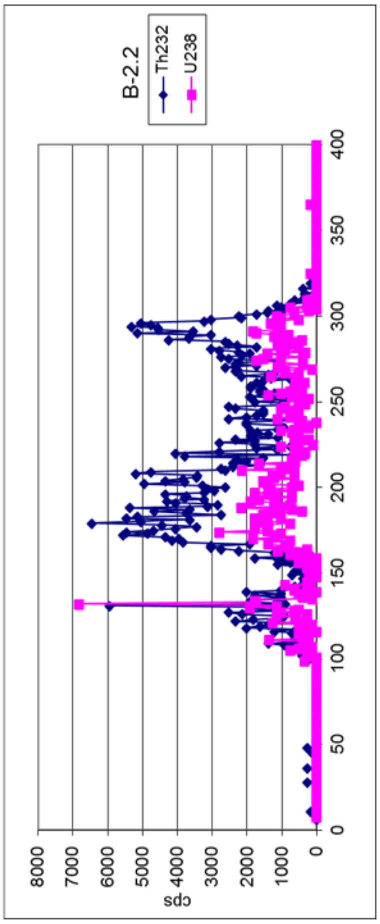
B-2.2
Th232
U238
cps
8000
7000
6000
5000
4000
3000
2000
1000
0
0
50
100
150
200
250
300
350
400

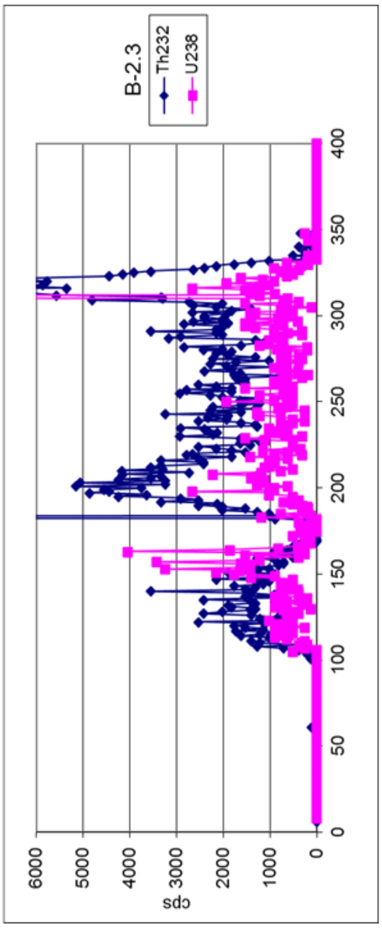
B-2.3
Th232
U238
cps
6000
5000
4000
3000
2000
1000
0
0
50
100
150
200
250
300
350
400

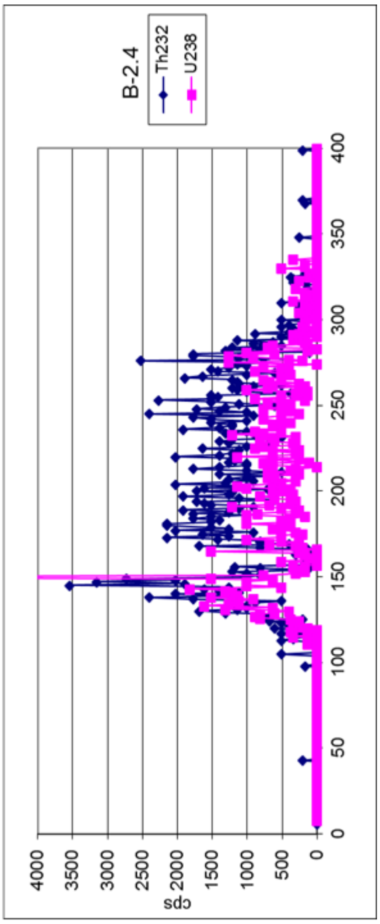
B-2.4
Th232
U238
cps
4000
3500
3000
2500
2000
1500
1000
500
0
0
50
100
150
200
250
300
350
400

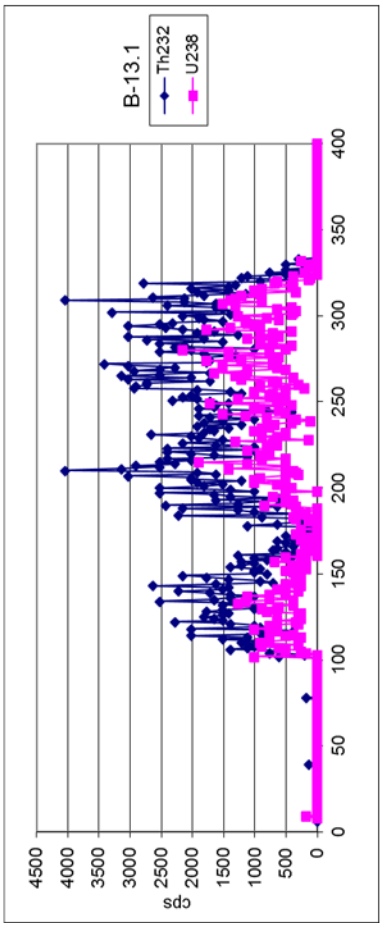
B-13.1
Th232
U238
cps
0
500
1000
1500
2000
2500
3000
3500
4000
4500
0
50
100
150
200
250
300
350
400

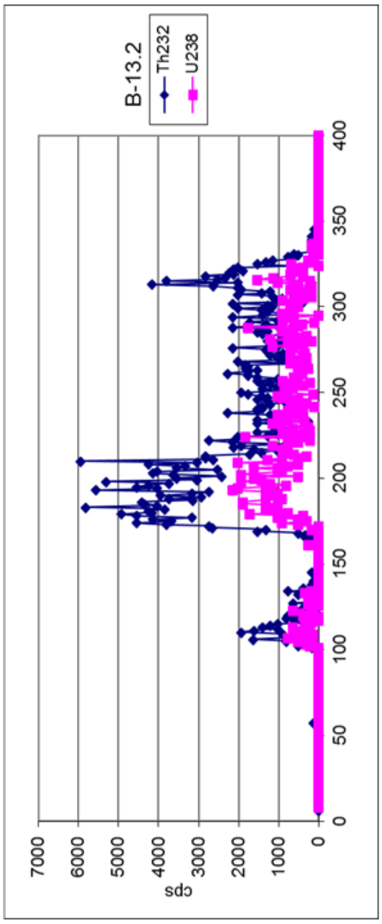
B-13.2
Th232
U238
cps
0
1000
2000
3000
4000
5000
6000
7000
0
50
100
150
200
250
300
350
400

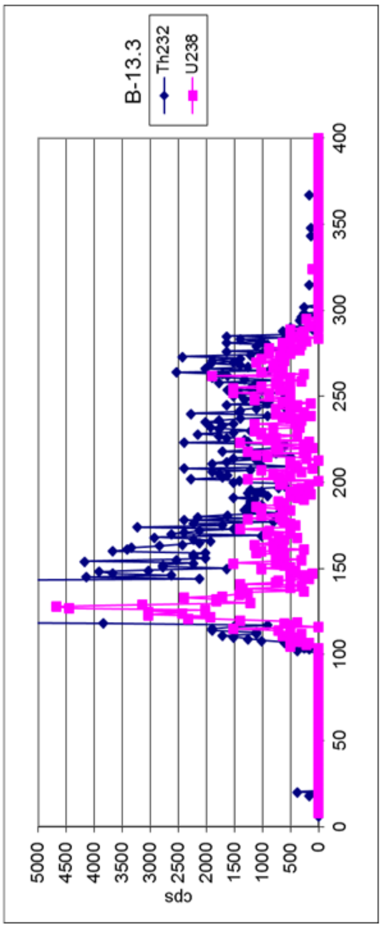
B-13.3
Th232
U238
cps
0
500
1000
1500
2000
2500
3000
3500
4000
4500
5000
0
50
100
150
200
250
300
350
400

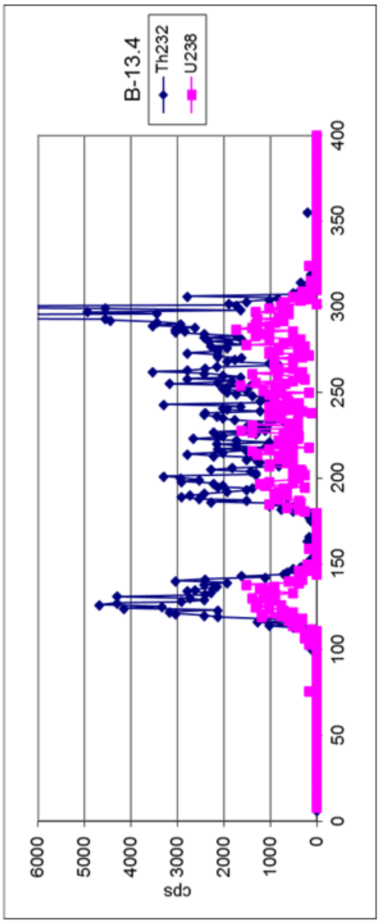
B-13.4
Th232
U238
cps
0
1000
2000
3000
4000
5000
6000
0
50
100
150
200
250
300
350
400

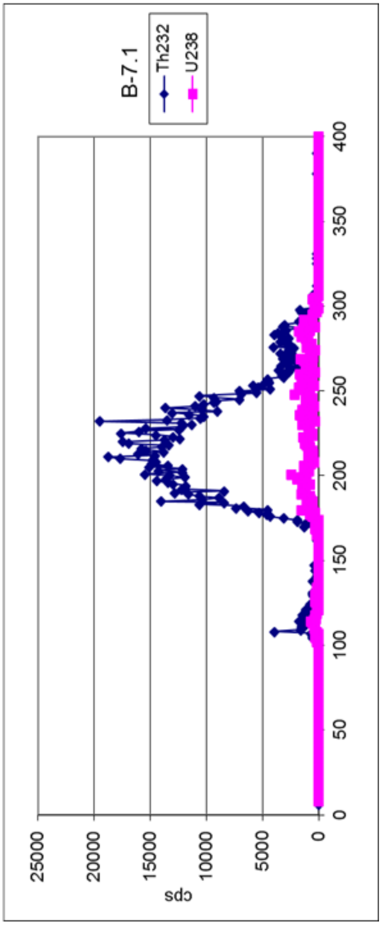
B-7.1
Th232
U238
cps
0
5000
10000
15000
20000
25000
0
50
100
150
200
250
300
350
400

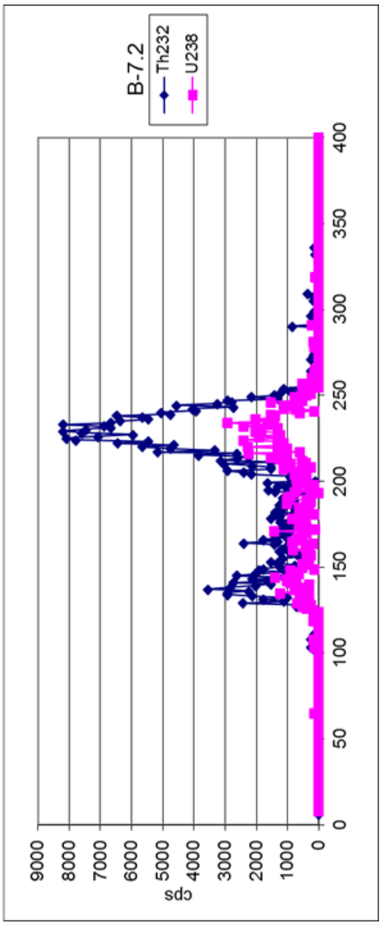
B-7.2
Th232
U238
cps
0
1000
2000
3000
4000
5000
6000
7000
8000
9000
0
50
100
150
200
250
300
350
400

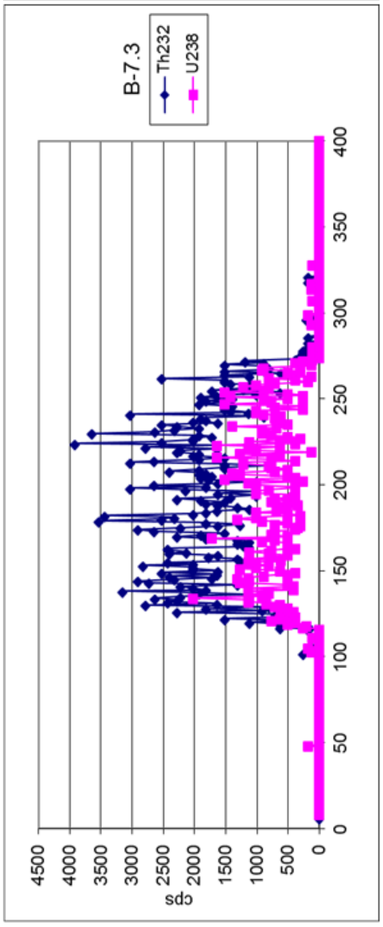
B-7.3
Th232
U238
cps
0
500
1000
1500
2000
2500
3000
3500
4000
4500
0
50
100
150
200
250
300
350
400

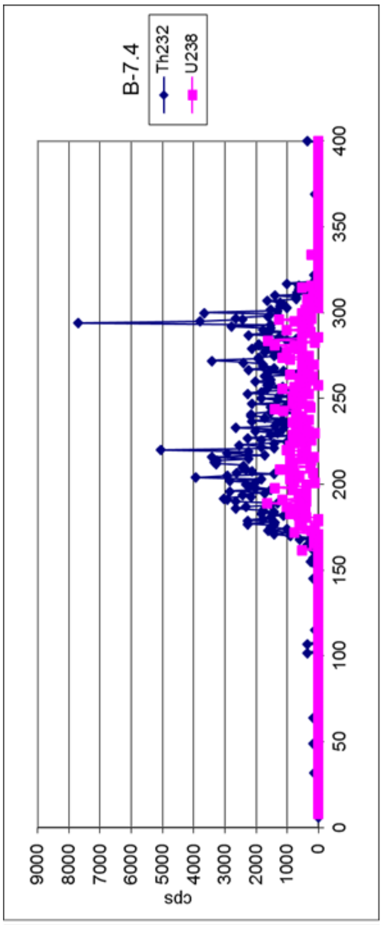
B-7.4
Th232
U238
cps
0
1000
2000
3000
4000
5000
6000
7000
8000
9000
0
50
100
150
200
250
300
350
400

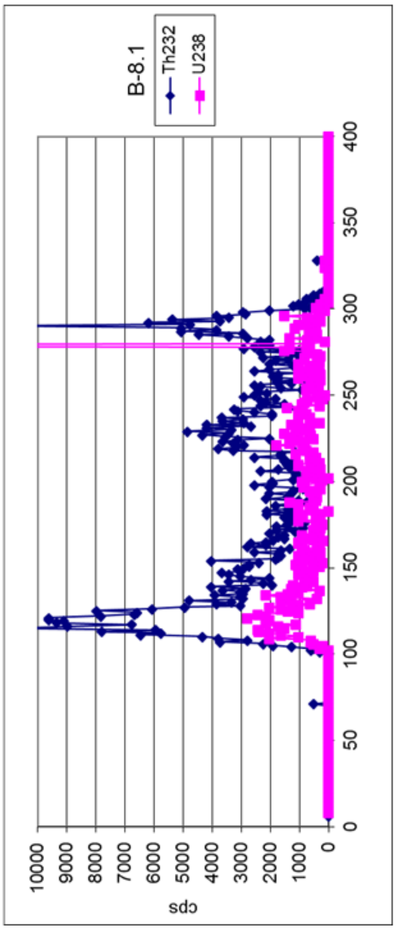
B-8.1
Th232
U238
cps
0
1000
2000
3000
4000
5000
6000
7000
8000
9000
10000
0
50
100
150
200
250
300
350
400

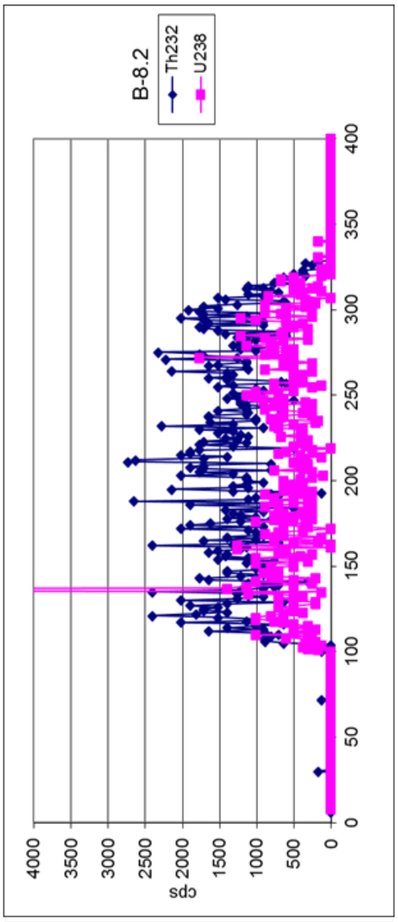
B-8.2
Th232
U238
cps
0
500
1000
1500
2000
2500
3000
3500
4000
0
50
100
150
200
250
300
350
400

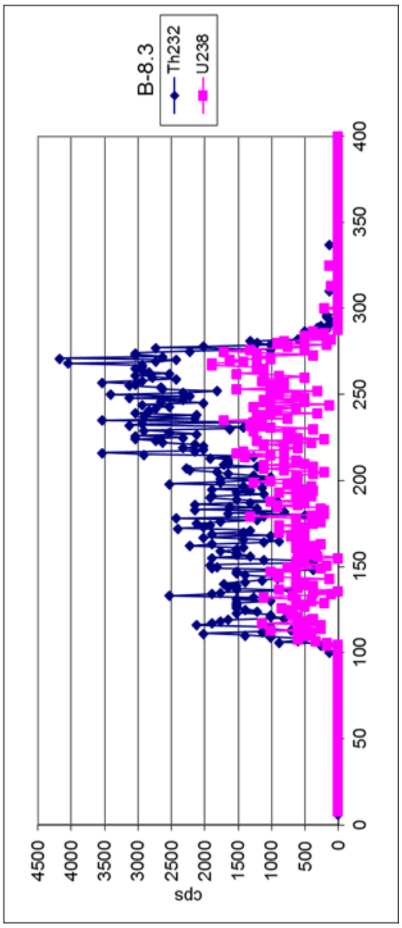
B-8.3
Th232
U238
cps
0
500
1000
1500
2000
2500
3000
3500
4000
4500
0
50
100
150
200
250
300
350
400

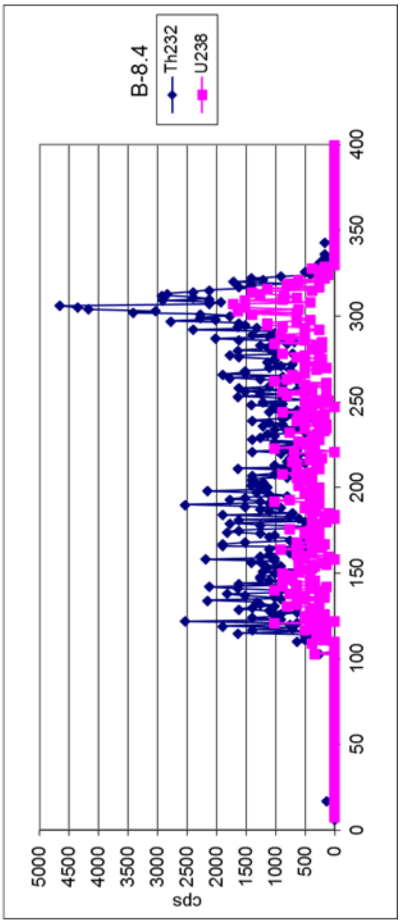
B-8.4
Th232
U238
cps
0
500
1000
1500
2000
2500
3000
3500
4000
4500
5000
0
50
100
150
200
250
300
350
400

Concordia plots of U-Pb age of samples B-2, B-8 and B-9 from May 27th 2016 provided by István Dunkl

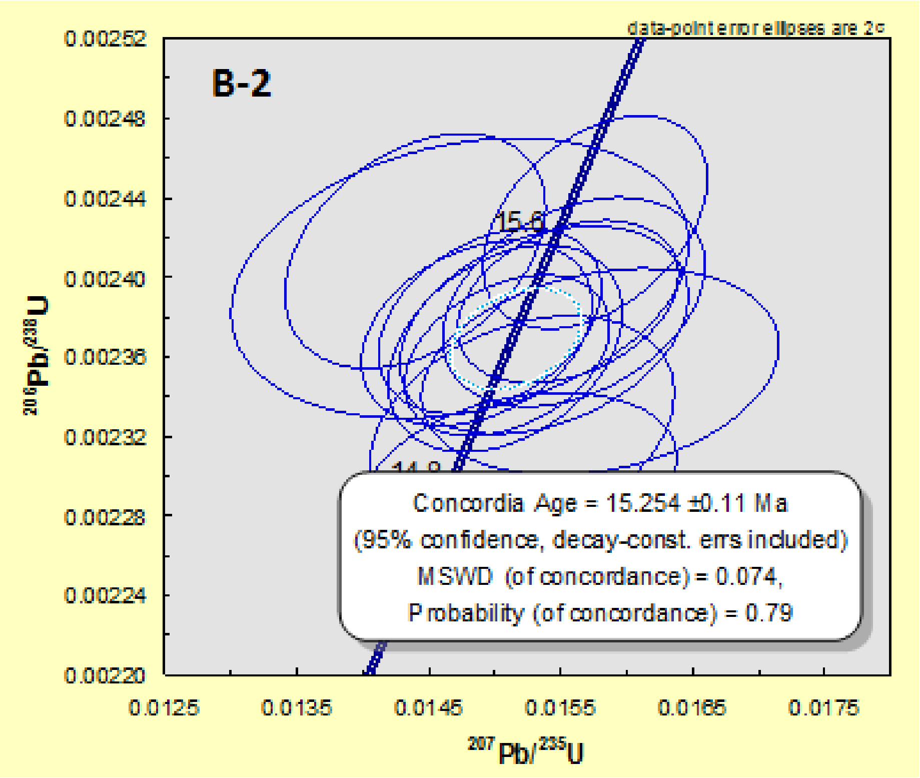

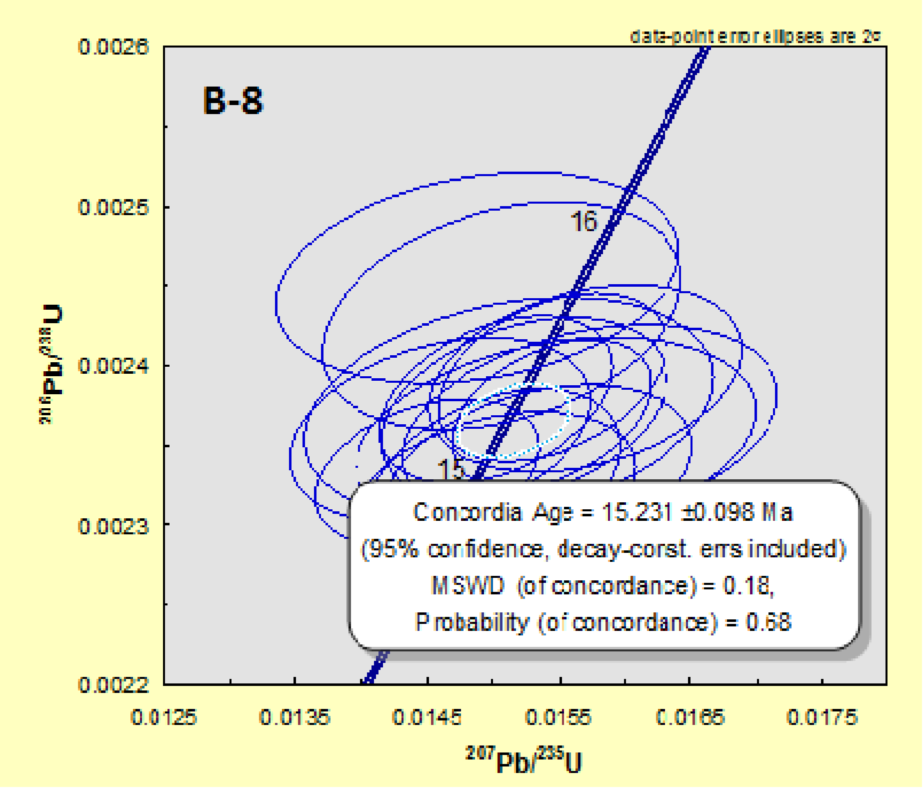

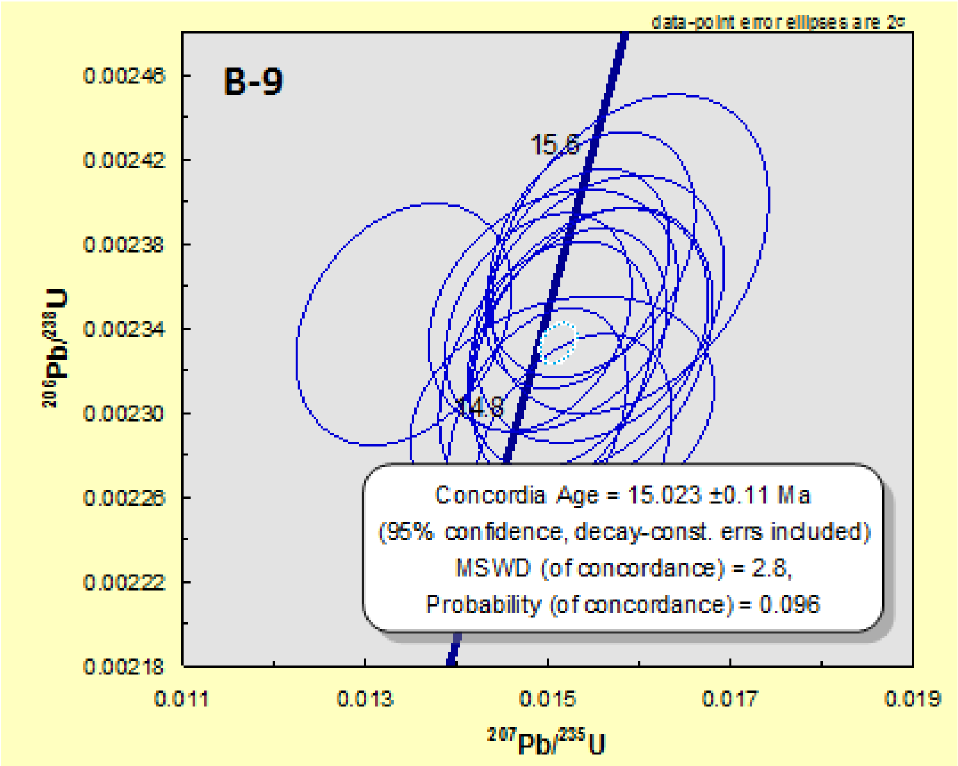
data-point error ellipses are 2σ
B-9
15.6
14.8
Concordia Age = 15.023 ±0.11 Ma
(95% confidence, decay-const. errs included)
MSWD (of concordance) = 2.8,
Probability (of concordance) = 0.096
0.00246
0.00242
0.00238
0.00234
0.00230
0.00226
0.00222
0.00218
^{206}Pb/^{238}U
0.011
0.013
0.015
0.017
0.019
^{207}Pb/^{235}U